UNIVERSITY OF COPENHAGEN
FACULTY OF SCIENCE

Master Thesis

Nicolas K. V. Grunwald

Impact of the Greenland Telescope relocation on future Event Horizon Telescope observations

Supervisor: Jes K. Jørgensen & Darach J. Watson

Submitted on: 20th May 2021

Impact of the Greenland Telescope relocation on future Event Horizon Telescope observations

Nicolas K. V. Grunwald
nwf125@alumni.ku.dk

Advisors: Jes K. Jørgensen & Darach J. Watson

May 2021

Abstract

Very Long Baseline Interferometry (VLBI) radio observations in the mm-regime allow for resolutions capable of resolving the shadow of the supermassive black hole in the center of Messier 87. The progression toward higher frequency observations allows for greater insight into jet-formation mechanics at horizon scales, as well as testing of Einstein's theory of General Relativity in the most extreme of gravitational environments. As the Event Horizon Telescope (EHT) approaches capabilities for 345 GHz observations, the Greenland Telescope (GLT) is proposed to be relocated from Thule to the Summit Camp, central Greenland 3.2 km above sea level, in an attempt to expand VLBI possibilities at the highest frequencies. The aim of this M.Sc. thesis project is to explore what is gained by including GLT in the EHT network and what further advantages, in particular for image quality, can be achieved by relocating the telescope to the Summit Camp. I will simulate 230 GHz and 345 GHz observations of an M87* model, using the simulation software `eht-imaging` and clean my data using the visibility imaging software DIFMAP, probing both the inclusion, as well as the relocation of GLT. I use existing atmospheric opacity data alongside a synthetic atmospheric transmission spectra generation tool to estimate the expected 230 GHz and 345 GHz receiver upgrade for the Greenland Telescope and a variety of technical documents as well as sensitivity estimators to estimate capabilities of the remaining EHT stations. The proposed new GLT site, the Summit Camp, will ensure better year-round performance for the telescope. Estimated summer-season atmospheric transmissions are better than the old site's winter-season transmissions and significantly widen the limited use of the 345 GHz receiver, which improves sensitivity of simulated 345 GHz EHT campaigns slightly. Simulated EHT observation with GLT at Thule show that thermal noise is not a limiting factor in observing M87* through 345 GHz radiation, but the current GLT site may be limited in performing VLBI observations by atmospheric fluctuations. Recovered image quality is significantly bettered by the inclusion of GLT, but mostly unaltered by the relocation, due to similar uv-coverage.

Contents

1 Introduction

In April of 2019 a team of astronomers presented the first ever high resolution image of the shadow of a supermassive rotating black hole (The EHT Collaboration et al. [2019a]). The observation was performed by utilizing antennae located all over the Globe as a very

Figure 1: Recovered image from the 2017 Event Horizon Telescope 1.3mm observation of the nucleus of Messier 87 (The EHT Collaboration et al. [2019a]).

long baseline interferometry (VLBI) array, collecting and correlating 1.3mm, or 230 GHz, radiation originating from the nucleus of the large elliptical galaxy Messier 87 (M87) - a particularly interesting galaxy due to its immense mass and relative close proximity. This momentous achievement in observational radio astronomy allowed for the most detailed structure study of such a compact object to date and does not only serve as an opportunity to study the behavior of photons in extreme gravity at scales of the event horizon of a black hole, serving as an important test of the theory of General Relativity. It also allows for the high resolution study of a region presumed to be the origin of an astrophysical jet. The formation mechanics of active galactic nuclei (AGN) outflows are still debated to this day, but are believed to be either produced by extraction of rotational energy from the central supermassive black hole (Blandford and Znajek [1977]) or that the jet is a magnetically collimated wind originating from the surrounding accretion disk flow (Blandford and Payne [1982]).

The measured wavelength of any observation impacts the achievable resolution. Globe-spanning interferometric campaigns collecting radiation from the radio core at progressively higher frequencies (≥ 230 GHz) allow for observations at resolutions down to $\sim 10\mu$as, which

has the resolving power to obtain a resolved view of the black hole event horizon. Most of the sites of the individual telescopes included in the Event Horizon Telescope (EHT) are believed to have sufficiently good conditions such that 345 GHz observations are possible for at least for parts of the year, but each site is affected by certain challenges as the telescope receiver frequency is tuned higher. A major concern is atmospheric weather conditions - water vapor content and atmospheric fluctuations. One site in particular is thought to be very limited by these effects, namely the location of the Greenland Telescope near the Thule Air Base, northwestern Greenland.

The Greenland Telescope (GLT) is a single dish 12 meter diameter radio telescope. It was granted to the Smithsonian Astrophysical Observatory (SAO) by the U.S. National Science Foundation (NSF) in 2011 with the intent that it was to be integrated into the Event Horizon Telescope network. The antenna was originally named the "North American ALMA (Atacama Large Millimeter Array) prototype antenna" and was tested at the Very Large Array (VLA) site in New Mexico. The tests were deemed successful and Vertex RSI began producing 12 meter arrays for the ALMA telescope, using the prototype as the model. The prototype was then put up for adoption, later to be owned by SAO in collaboration with Academia Sinica in Taiwan, who installed the prototype in Greenland after which the telescope is now named.

In this thesis, I will present my analysis of the future capabilities of the Event Horizon Telescope with particular focus on the relocation of the northern-most node, the Greenland Telescope. My work includes building a robust understanding of how radio-interferometers work as well as gathering the necessary tools, and the knowledge to operate them, for use in simulating, editing and imaging synthetic VLBI data. I will need to understand what mechanisms produce radio wavelength emission near a supermassive black hole, in order to interpret what is observed at varying frequency bands. I will construct my own array configurations using information from the 11 concurrent EHT stations as well as gathering information about the relocation of the Greenland Telescope and what effect this will have on the sensitivity of the single-dish telescope and EHT as a whole. Utilizing my configurations, I will simulate 230 GHz, 345 GHz and 650 GHz observations of M87* with the Event Horizon Telescope and asses the general capability as well as the impact of the GLT relocation with regard to recoverable image, noise and S/N ratios. Furthermore, I will also explore single baseline capabilities using correlated flux estimations based on visibility samples from my simulations.

2 Theory

In this section, I will present an outline of radio astronomy and interferometry. I will draw heavily upon the mathematics and ideas as presented in *Essential Radio Astronomy*

(ERA) (Condon and Ransom [2016], sections 3.2-3 + 3.7) and *Interferometry and Synthesis in Radio Astronomy* (ISRA) (Thompson et al. [2017]), as well as the online webinar *VLBI Data Series* available on YouTube[1]. To fully appreciate the theory, I will provide supporting figures both from the books as well as my own calculations.

2.1 Radio antennae

Single dish radio telescopes must be build exceedingly large to achieve resolutions comparable to those in other astronomical wavelengths. By analyzing the power pattern of a uniformly lit aperture (Condon and Ransom [2016], p.89), the diffraction limited resolution - or *half-power beam width*[2] - of a radio telescope can be estimated as

$$\theta_{\mathrm{HPBW}} \approx 0.89 \frac{\lambda}{D} \tag{1}$$

where D is the diameter of the antenna and λ is the measured wavelength. For centimeter-size wavelengths, in order to achieve a resolution of $2''$, one would require a radio dish several kilometers across. While building very large radio dishes is in no way impossible (Nan et al. [2011]), the required size for high angular resolution, i.e. sub-arcsecond observations, extends beyond current mechanical engineering and "filled-aperture" radio telescopes. This size boundary can be overcome by the use of aperture-synthesis interferometry.

Paraboloidal, or *parabolic*, reflectors are commonly used at the short radio wavelength end of the observing spectrum. These collect and focus radiation from a source into a single focal point, which is then subsequently amplified and recorded. Parabolic antennae come in different shapes and sizes, some of the most common are shown in Fig. 2. The name *paraboloidal* refers to the distinct geometry of the reflector that ensures each part of the incoming radiation wavefront is reflected such that all information reach the focal point at the same time. In other words, the *path length* from primary reflector to focal point is constant across the dish, which keeps all parts of the incoming plane wavefront in phase. By studying the geometry (Condon and Ransom [2016], section 3.2.1) of the parabolic reflector, the equation of a paraboloid with focal length f can be expressed as

$$z = \frac{r^2}{4f} \tag{2}$$

with r being the radial offset from the centre of the dish, and z, the height. Any deviation from this shape will introduce errors in the measurement of the signal, caused by corruption of the incoming wavefront phase. For larger antenna sizes, maintaining perfect curvatures becomes more difficult, especially in regard to higher frequency radiation[3] which is much

[1] `https://www.youtube.com/channel/UCPrigv3Rt9kLrt1J_ywf3kg`

[2] It is common to measure the angle between points of half-power on the main beam. This is also referred to as the full width between half max (FWHM).

[3] For a list of other technical concerns, see: `http://www.astrosurf.com/luxorion/dish-antenna-building.htm`

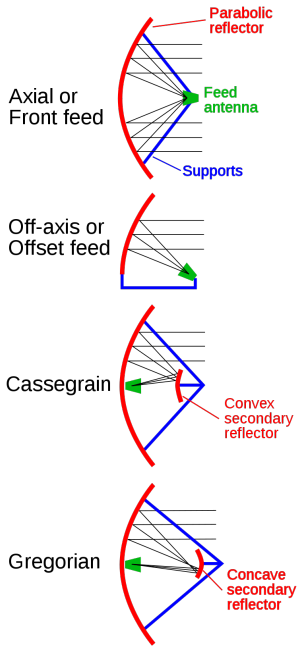

Figure 2: Four common types of parabolic reflector antennas. Always present is a *primary reflector* and a *feed antenna*, though some variants, such as the Cassegrain reflector, also includes a *secondary reflector* suspended above the primary reflector, increasing the focal length. (Image by **Chris Burks**: `https://en.wikipedia.org/wiki/Parabolic_antenna`)

more sensitive to surface errors due to the shorter wavelength. The focal ratio f/D of the antenna is the ratio of the focal length and diameter of the primary reflector. The focal ratio of radio antennae is usually smaller than those of optical telescopes by about one order of magnitude (Condon and Ransom [2016], p. 81), due to the large dish-sizes. A decrease in f/D is analogous to a decrease in field-of-view, or FOV. Radio telescopes are thus limited, compared to observations in optical wavebands, in the area of the sky that can be observed at any given time. The common use of paraboloidal reflectors in radio astronomy can be attributed to three main factors: Firstly, these types of telescopes are comparatively simple as opposed to other configurations such as phased arrays. Secondly, the collecting area of a reflector antenna closely matches the geometric area of the primary reflector. Finally, these telescopes can work over a wide range of frequencies, due to the easily switched antenna feed, allowing for different wavelength observations without requiring multiple telescopes (Condon and Ransom [2016], p. 81).

In most cases, the received signal from cosmic sources can be approximated as planer across the reflector. The curvature of the dish largely becomes a non-factor and the collecting

area can be assumed to be the circular projection of the antenna, onto the *aperture plane* (Condon and Ransom [2016], section 3.2.2) - see Fig. 3. This approximation holds only

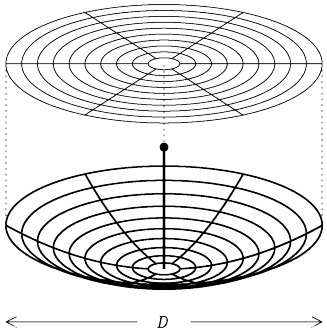

Figure 3: Circular projection of a paraboloidal reflector with diameter D onto the aperture plane (Figure from Condon and Ransom [2016], p. 83).

insofar as the observed signal originates at a distance away, R, that satisfies $R \gg R_{\rm ff}$, where $R_{\rm ff}$ is the *far-field distance* defined as

$$R_{\rm ff} \approx \frac{2D^2}{\lambda} \tag{3}$$

depending on both the reflector size and measured wavelength. For correlated signals between two or more antennae, separated by a distance, b, the far field approximation simply holds if

$$R \gg b. \tag{4}$$

This distance is also refereed to as the *baseline distance*, with one pair of antennae forming a single baseline. For configurations including N dishes of size d we can approximate the total collecting area as

$$A_{\rm tot} = N\pi(d/2)^2 \tag{5}$$

with an equivalent single synthesized dish of diameter

$$D_{\rm syn} = N^{1/2}d. \tag{6}$$

As an example, the phased ALMA array[4] (Goddi et al. [2019]) consists of fifty 12 meter diameter antennae (the "12 meter Array") and an additional twelve 7 meter diameter and four 12 meter diameter antennae (the "Atacama Compact Array", or "ACA"). The 12 meter Array can act as one giant aperture of size

$$(50)^{\frac{1}{2}}12\text{m} \approx 85\text{m} \tag{7}$$

[4]ALMA configuration which allows for coherent summing of all individual ALMA antennae signals, allowing the array to act as a single high-resolution telescope.

with a total collecting area of

$$50\pi(12\text{m}/2)^2 \approx 5700\text{m}^2. \tag{8}$$

This calculation varies depending on which cycle of ALMA is used for the calculation, but it is immediately apparent that we can create, or *synthesize*, very large apertures by way of combining several antennae together. While this is an impressively huge collecting area, one must recall that ALMA has baselines that span upwards of 16 kilometers. An aperture-filled radio dish of this extent would have a staggering total collecting area of ~ 800 square kilometers. This means that the synthesized dish only covers a mere ~ 7 parts per million of the hypothetical aperture spanned by the maximally separated ALMA antennae. This has the important implication, that shall be explored in later sections, namely that not all information is recorded when using aperture-synthesis radio interferometry.

2.2 Aperture illumination

The *aperture* is the opening, or area, in which observed rays of light are being collected during an observation. These openings can vary in size and engineering and one example is the projection of the primary reflector onto the aperture plane, as discussed earlier and shown in Fig. 3, or simpler yet; the lens on a camera. An important property of radio antennae, is that most fundamental aspects remain the same when viewed either as a transmitter or receiver (Condon and Ransom [2016], section 3.1). In other words, the physics behind generating a signal for transmission, is identical to the physics measured when receiving a signal. Consider a one-dimensional antenna that extends from $x = -D/2$ to $x = D/2$, governed by a spatially dependant electric field strength $g(x)$, transmitting to some faraway receiver. Using the interactive geometry software Geogebra[5], I have sketched such a configuration, which can be seen in Fig. 4. The sketch is inspired by Condon and Ransom [2016], Figure 3.11. The *Huygens-Fresnel principle*[6] states that each point on a wavefront is in itself a source of spherical wavelets. The sum of all these individual wavelets is what constitutes the wavefront. Likewise the received signal from an antenna can be thought of as the sum of multiple signals generated by smaller antennae of size dx at position x. Let us place a receiver a large distance, R, away from the antenna, such that $R \gg R_{\text{ff}}$. The produced electric field from each antenna element at the location of the receiver would then be

$$df \propto \frac{g(x)}{r(x)} \exp(-i2\pi r(x)/\lambda)dx \tag{9}$$

with $r(x)$ being the distance between element and receiver. Since $R \gg R_{\text{ff}}$, the received signal will act as far-field radiation and the *Fraunhofer approximation* can be used to determine

[5] `https://www.geogebra.org/`

[6] `https://www.mathpages.com/home/kmath242/kmath242.htm`

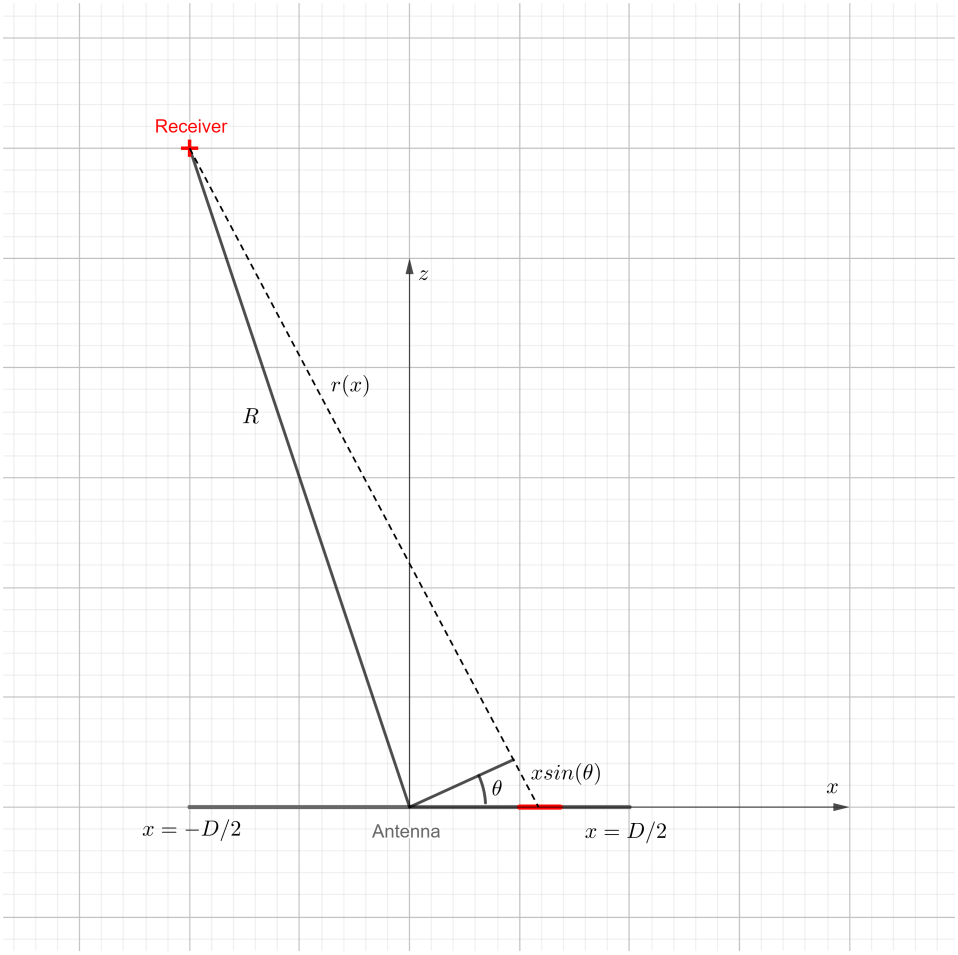

Figure 4: Sketch of a one-dimensional antenna of length D, transmitting to a faraway receiver (red cross) at a distance R. The received signal is the sum of individually produced signals from elements of the antenna, marked in red, a distance $r(x)$ away from the receiver.

that (Condon and Ransom [2016], p. 85)

$$r \approx R + xsin\theta \approx R + xl \qquad [l \equiv \sin\theta]. \tag{10}$$

For very large distances, the term $1/r(x)$ approaches a constant value across the transmitting antenna dish and can thus be absorbed into the constant of proportionality. Expanding eq. (9) using eq. (10) we get

$$df \propto g(x)\left[\exp(-i2\pi R/\lambda) + \exp(-i2\pi xl/\lambda)\right] dx \tag{11}$$

in which the first bracketed term is constant, thus:

$$df \propto g(x) \exp(-i2\pi xl/\lambda)dx. \tag{12}$$

Lastly, by defining

$$u \equiv x/\lambda \tag{13}$$

as an expression for position on the antenna in units of wavelength, one reaches the important conclusion

$$f(l) = \int_{\text{aperture}} g(u) \exp(-i2\pi lu)du \tag{14}$$

namely that **the far field radiation pattern of the antenna is equal to the Fourier transform of the electric field distribution across its aperture**. This can be generalized to two dimensions (Condon and Ransom [2016], section 3.3) as

$$f(l,m) \propto \int_{-\infty}^{\infty}\int_{-\infty}^{\infty} g(u,v) \exp(-i2\pi(lu+mv))dudv \tag{15}$$

with $l = \sin\theta_x$, $m = \sin\theta_y$ and $v \equiv y/\lambda$. This relation between antenna aperture illumination from a faraway source, and the resulting antenna power pattern, is used to interpret the measurement of the antenna - what the antenna *sees*. This result is very powerful and should be explored in an example.

2.3 Uniformly lit antenna Fourier analysis example

In the most simple case, one can imagine a one dimensional aperture with constant illumination $g(u)$ across the dish, i.e. a square pulse function

$$g(u) = \begin{cases} 1 & |u| < 1/2 \\ 0 & |u| > 1/2 \end{cases}. \tag{16}$$

Eq. (14) tells us that the electric field pattern $f(l)$ is the Fourier transform of the electric field distribution across the aperture. In this example the aperture is uniformly lit and the illumination thus extends from $u = -1/2$ to $u = 1/2$, so

$$\begin{aligned} f(l) &= \int_{-1/2}^{+1/2} g(u) \exp(-i2\pi lu)du = \\ &\int_{-1/2}^{+1/2} \exp(-i2\pi lu)du = \left[\frac{\exp(-i2\pi lu)}{-i2\pi l}\right]_{-1/2}^{+1/2} \end{aligned} \tag{17}$$

evaluating yields

$$f(l) = \frac{\exp(-i\pi l) - \exp(i\pi l)}{-i2\pi l} = \frac{-2i\sin(\pi l)}{-i2\pi l} = \frac{\sin(\pi l)}{\pi l}. \tag{18}$$

This result is also known as a *sinc* function. Furthermore the *power pattern* of the antenna is the equal to the field pattern squared. The central peak in the power pattern is refereed to as the *main beam* or *main lobe*, with subsequent smaller peaks dubbed the *side lobes*. When imaging, information stemming from the main lobe is desirable, while side lobes often create smudging or artifacts in the image. The resolution of a telescope is defined by the angular width of the main beam, though there exists some slight variety in how the resolution is defined, such as the half-power beam width[7] mentioned earlier (see eq. (1)). Using Python[8] I define and plot the illumination pattern function $g(u)$, field pattern $f(l)$ and power pattern $f(l)^2$. Results can be seen in Fig. 5.

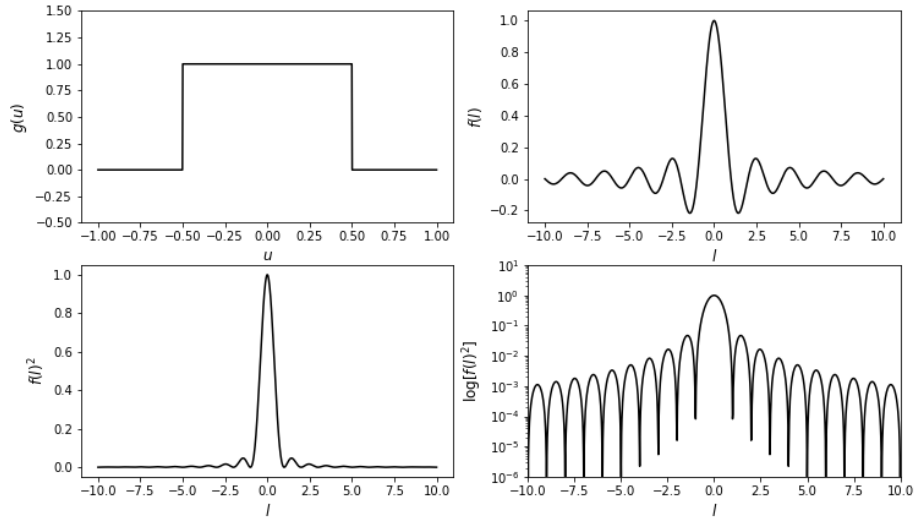

Figure 5: Aperture illumination $g(u)$, electric field pattern $f(l)$ and corresponding power pattern $f(l)^2$ for an evenly lit one-dimensional antenna aperture. The power pattern is plotted both on a linear and logarithmic scale.

This shows the application of using Fourier transformations for aperture analysis. Given an arbitrary aperture illumination pattern, we can calculate the corresponding electric field pattern on the sky. This also allows for the understanding and correction of effects from blockages such as supports suspending a secondary reflector or mirror above the primary aperture, a construction often used to increase focal length of telescopes. As a simple

[7] As the name suggests, this resolution is defined from the angular width between half-power points of the main lobe, as opposed to the angular width between the first two minima.

[8] `https://www.python.org/`

example, I use Python to create an image that represents an illuminated reflector dish shadowed by four supports that hold a secondary mirror. This image is then the aperture plane cross-section of the dish, normal to the viewing direction, where illuminated parts are white. I then Fourier transform the image matrix which produces the antenna field pattern, or *sky response* of the antenna. These images are shown in Fig. 6. The antenna pattern

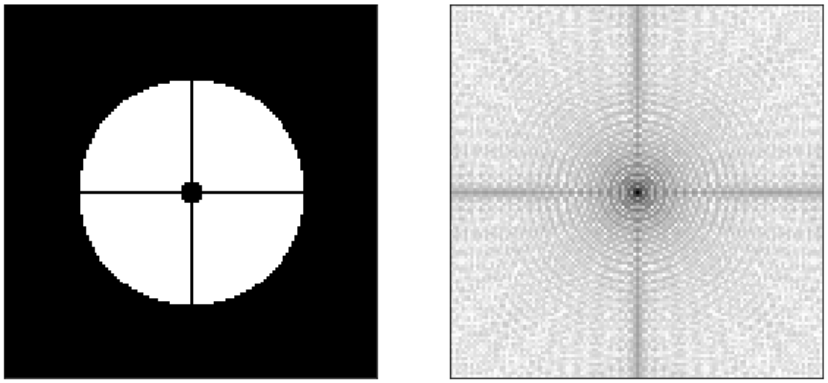

Figure 6: **Left:** Aperture plane representation of a circular aperture, shadowed by a secondary mirror / reflector suspended by four supports. The illuminated parts are white. **Right:** Discrete Fourier transform of the aperture illumination. The effects of the supports and secondary reflector manifest as horizontal and vertical lines around the central main lobe.

show clear horizontal and vertical spikes around the central main lobe. These effects explain *diffraction spikes* on images of stars, such as the ones shown in Fig. 7. Furthermore, the diffuse light surrounding the star is a product of the the side lobes, smudging the image. From these considerations, one could imagine that a *perfect* power pattern is simply a delta function, with infinite resolution and no side lobes, even though this is purely hypothetical.

2.4 Radio interferometry

The need for interferometry mainly stems from engineering limitations, but does have certain advantages over the usage of single dish telescopes. As already mentioned, building large radio antennae requires extreme precision when shaping the dish, lest the phase of the signal be corrupted by an uneven surface. Maintaining the paraboloid shape is easier if the antenna is small, thus the problem of antenna accuracy becomes easier to manage if the array is composed of several smaller antennae. The use of multiple antennae also allows for

Figure 7: Picture of the star Antares in the constellation Scorpius. In this case the diffraction spikes are the product of a simple wire cross, fixed in front of the aperture, for demonstration purposes. (**Credit: Cory Schmitz** (`http://photographingspace.com/howto-diffraction-spikes/`))

baselines separations, b, much longer than the extend of any single dish telescope, which allows for much improved resolution, scaling as

$$\theta \propto \frac{\lambda}{b}. \tag{19}$$

Note the similarity between this equation and eq. (1). Interferometers also boast some of the largest collecting areas of any telescopes, as explored in the ALMA example in the previous section. Astrometric precision is also much improved, as source positions on the sky are determined by phase difference in the measured signal across different antennae and *not* the steering of a single dish telescope. While all these factors certainly are major improvements, interferometric measurements have one major drawback; *missing information*. The synthesized aperture is not "filled" and functions, in a sense, like a radio dish with (a lot of) missing patches. Effects of these missing patches, and how to deal with them, will be explored later. This section will outline the physics of the interferometric measurement.

Consider two antennae separated in the East-West direction by a baseline distance, b, observing far field radiation from a distant monochromatic point source at some angle, θ, normal to the ground. The incoming radiation can be approximated as plane waves and will for $|\theta| > 0$ reach one antenna before the other, introducing a *geometric time delay*

$$\tau_g = \frac{b \sin \theta}{c} \tag{20}$$

with c being the speed of light. Measured signals are *correlated*, often by way of multiplying and time-averaging, which filters out high frequency components (Thompson et al. [2017], p. 60). The closest antenna will measure a signal $V_1 = V \cos[2\pi\nu(t - \tau_g)]$, with V being the

induced voltage. The furthest antenna will shortly after measure the signal $V_2 = V\cos[2\pi\nu t]$. The signals are then correlated, yielding the time-averaged signal F

$$F = \langle V_1 V_2 \rangle = V^2 \langle \cos[2\pi\nu t]\cos[2\pi\nu(t-\tau_g)]\rangle. \tag{21}$$

The cosine term can be re-written as

$$\begin{aligned} &V^2\langle\cos[2\pi\nu t]\cos[2\pi\nu(t-\tau_g)]\rangle \\ &= \frac{V^2}{2}\langle\cos[2\pi\nu\tau_g] + \cos[4\pi\nu t - 2\pi\nu\tau_g]\rangle. \end{aligned} \tag{22}$$

The second time-averaged term $\cos[4\pi\nu t - 2\pi\nu\tau_g]$ will equal zero for even short time measurement. On the contrary, the geometric time delay varies slowly as the Earth rotates and does not equal zero when time averaged. Using eq. (20), the correlated signal can be written as

$$F = \frac{V^2}{2}\cos(2\pi\nu\tau_g) = \frac{V^2}{2}\cos\left(\frac{2\pi\nu}{c}b\sin\theta\right) = \frac{V^2}{2}\cos\left(2\pi\frac{b}{\lambda}\sin\theta\right) \tag{23}$$

where we can once again use the definition, that $l \equiv \sin\theta$ to find that the correlated signal measured between two antennae create the *fringe pattern*

$$F = \frac{V^2}{2}\cos\left(2\pi l\frac{b}{\lambda}\right) \tag{24}$$

created by the interference between the two signals. Constructive interference, i.e. fringe pattern maxima, happens when the signals exhibit similar phase, and destructive interference, i.e. fringe pattern minima, happens when the signals are out of phase. The fringe pattern oscillations are - for a fixed baseline and wavelength - determined by the source position on the sky, as this relates to the geometric time delay and, by proxy, the phase difference between the two signals. I have plotted an example of a fringe pattern for $V = 1$ and $b/\lambda = 3$ displayed in Fig. 8, in which the absolute value $|F|$ is plotted as the radial component. Cosmic sources are rarely monochromatic and antenna pass-bands have an important impact on the fringe pattern. To understand the effect, we simply integrate eq. (24) over a range of frequencies (Thompson et al. [2017], eq. (2.4))

$$\begin{aligned} F &= \frac{1}{\Delta\nu}\int_{\nu_0-\Delta\nu/2}^{\nu_0+\Delta\nu/2}\frac{V^2}{2}\cos\left(\frac{2\pi\nu b}{c}\sin\theta\right)d\nu \\ &= \frac{V^2}{2}\cos\left(\frac{2\pi\nu_0 b}{c}\sin\theta\right)\frac{\sin(\frac{\pi b\Delta\nu}{c}\sin\theta)}{\frac{\pi b\Delta\nu}{c}\sin\theta} \end{aligned} \tag{25}$$

which can be simplified greatly, by defining F_{ν_0} as the correlated monochromatic signal, and using the identity for the geometric time delay and the sinc function

$$F = F_{\nu_0}\mathrm{sinc}(\tau_{\mathrm{g}}\Delta\nu). \tag{26}$$

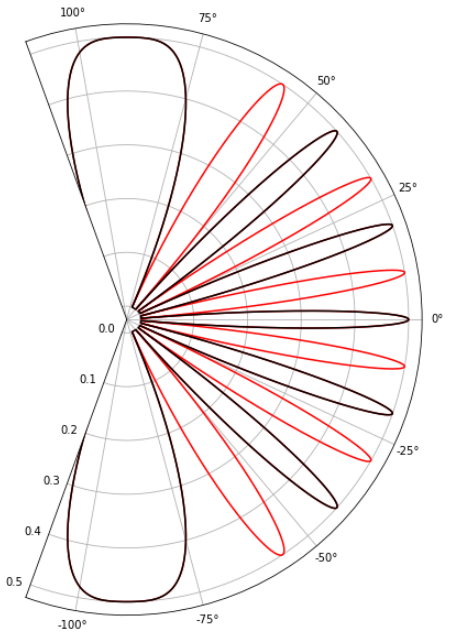

Figure 8: Polar plot of fringe pattern $F = V^2/2\cos(2\pi lb/\lambda)$. The absolute value $|F|$ is displayed for simplicity. The value of V has been set to 1, and the value of b/λ has been set to a very low 3 (This is not very true-to-life, but does greatly simplify the plot visually). Black lobes correspond to positive fringe amplitude, while red bands correspond to negative fringe amplitudes. The fringe width increases for large $|\theta|$, which is related to projected baseline shortening, decreasing the resolution.

This holds true if the band-pass is *rectangular*, i.e. the response is uniform to all frequencies within the sharply defined band-pass, but other solutions exist for different types. In every case, the band-pass gives rise to an envelope function that envelopes the fringe pattern. In this case, if either the geometric time delay is large, or the band-pass is very wide, the correlated signal will fade at certain positions on the sky, which is not optimal. A simple visual example of this can be seen in Fig. 9, where the the original fringe pattern has been convolved with a $\mathrm{sinc}(\sin\theta)$ function, as $\tau_g \propto \sin\theta$. Information beyond ± 50 degrees is no longer available due to the effects of the band-pass which tapers the fringe amplitude for increasing $|\theta|$ away from the *zero delay* (central lobe).

As $\tau_g \propto b$, the problem worsens for long baselines, which creates a necessity for *delay*

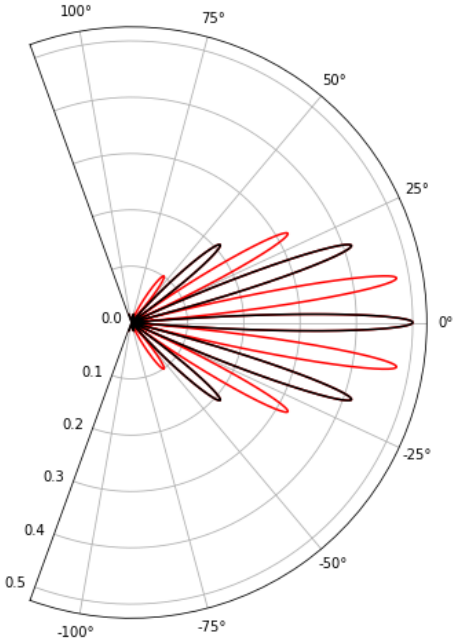

Figure 9: Polar plot of fringe pattern convolved with a sinc envelope $F = V^2/2\cos(2\pi lb/\lambda)\mathrm{sinc}(\sin\theta)$. The absolute value of $|F|$ is displayed for simplicity. The value of V has been set to 1, and the value of b/λ has been set to a very low 3 (This is not very true-to-life, but does greatly simplify the plot visually). Black lobes correspond to positive fringe amplitude, while red bands correspond to negative fringe amplitudes. The fringe amplitude tapers for increasing $|\theta|$ as a consequence of the band-pass.

tracking - a way of minimizing the impact of the envelope, by way of introducing *internal* time delay τ_i, such that $\tau = \tau_g - \tau_i$, where τ is the total time delay between stations. Precise knowledge of each antenna's location allow for estimates of the geometric delay, to which the internal delay is tuned as close as possible, such that $\tau_i \sim \tau_g$ and $\tau = 0$. This will lessen the effect of the envelope function, which will recover fringe amplitudes across the sky and allow for wider bandwidths $\Delta\nu$. When observing, it is commonplace to choose a *reference position* on the sky, at the location of the source. In one dimension this could be defined as θ_0 and the internal time delay would correspondingly be adjusted to $\tau_i = (b/c)\sin\theta_0$. The

correlated signal recorded from a position $(\theta_0 - \Delta\theta)$ on the sky would be proportional to

$$F \propto \cos(2\pi\nu_0\tau) = \cos\left[2\pi\nu_0\left(\frac{b}{c}\sin(\theta_0 - \Delta\theta) - \tau_i\right)\right] \tag{27}$$

which, by inserting the tuned interal time delay τ_i yields

$$F \propto \cos[2\pi\nu_0(b/c)\sin\Delta\theta\cos\theta_0] \tag{28}$$

for small $\Delta\theta$ (which is a fair assumption for very distant cosmic sources). The projected baseline separation normal to the observing direction $(b\cos\theta_0)$ affects the zero delay fringe width, or angular resolution, of the interferometer. For convenience we define

$$u \equiv \frac{1}{\lambda}b\cos\theta_0 = \frac{\nu_0}{c}b\cos\theta_0 \tag{29}$$

which is the projected baseline distance in units of wavelength. When observing close to the reference position we can assume $\tau \sim 0$ which lessens the effects of band-pass tapering and the signal measured becomes proportional to

$$F(l) \propto \cos(2\pi ul) \tag{30}$$

where both u and $l \equiv \sin\Delta\theta$ have been substituted into eq. (28) above. This is the interferometer response to a point source at position $\theta = \theta_0 - \Delta\theta$, with zero delay centered at θ_0. The quantity u is the *spatial frequency* most commonly measured in rad^{-1} (cycles per radian).

The one-dimensional response of an interferometer can be expressed as a convolution between the interferometer power pattern and some one dimensional intensity distribution across the sky $I_1(l)$ (Thompson et al. [2017], eq. (2.17)). The interferometer power pattern is a product of three factors. The *fringe patter*n, which we know to be a cosine with arguments u and l [see eq. (30)]. The *antennae power patterns*, denoted $A(l)$, explored in the previous section and equal to the squared Fourier transform of the antennae aperture illumination. Lastly, the *band-pass envelope* denoted $F_B(l)$, related to bandwidth shape and size:

$$R(l) = \int_s \cos[2\pi u(l' - l)]A(l')F_B(l')I_1(l')dl'. \tag{31}$$

This representation shows that for a given interferometer response, we can calculate the antenna power patterns as well as the band-pass envelope function, and thus information about the source intensity profile $I_1(l)$ can be recovered. The recovery of the source intensity distribution from interferometer response is called *image synthesis*. Usually the source extent on the sky is small compared to the antennae beam patterns $A(l)$ and the band-pass envelope pattern $F_B(l)$, in which case these will yield constant values across the sky, and we can omit them and rewrite the convolution above as

$$R(l) \sim \cos(2\pi ul) * I_1(l) \tag{32}$$

denoting a convolution between the antenna cosine response and the intensity distribution on the sky. Using the *convolution theorem* (Thompson et al. [2017], section 2.3.2), which states

$$\mathcal{F}[f * g] = \mathcal{F}[f] \cdot \mathcal{F}[g] \tag{33}$$

we can find the Fourier transform of the interferometer response $r(u) = \mathcal{F}[R(l)]$, namely the response as a function of projected baseline separation, by simply transforming each term individually and multiplying the results. The Fourier transform of the intensity distribution is called the *visibility function* and is denoted $\mathcal{V}(u)$. The visibility function is an integral part of interferometric imaging. It represents the complex amplitude and phase of the sinusoidal component of the intensity profile with spatial frequency u (Thompson et al. [2017], p. 69)). By carrying out the Fourier transform for a specific spatial frequency $u = u_0$, we get

$$\mathcal{F}[R(l)] = \frac{1}{2}[\mathcal{V}(-u_0)\delta(u + u_0) + \mathcal{V}(u)\delta(u - u_0)] = r(u) \tag{34}$$

where the delta function comes from the Fourier transform of the cosine term. This equation reveals a very import truth for interferometric measurements:

As an interferometer measures a sample on the sky, it measures the complex visibility $\mathcal{V}(\pm u)$, which is the Fourier transform of the intensity distribution on the sky, but only at the spatial frequency determined by the projected baseline separation of the antennae, u_0. The complex visibility exhibits both an amplitude and phase, associated with the measured spatial frequency. The former tells of the intensity amplitude and the latter informs of direction. By inverse Fourier transforming measured visibility samples we can recover information about the source intensity distribution at scales otherwise unresolved by single-dish telescopes.

From a single sample, the inverse Fourier transformation of the measured visibility holds very limited information about the source intensity distribution. Many samples are needed in order to realistically recover any information, or *structure*, in the image. This reality ties back into the discussion in the prior section. Even though interferometers have much larger collecting areas and improved resolution, it comes at the cost of information. Before touching on how to best circumvent this issue, I'll quickly cover geometric considerations with regard to interferometric sampling and the so-called "uv-plane".

2.5 Geometric considerations and uv-coverage

In this section I will paint a picture of an interferometric observation, which will set the stage for the simulations in the later sections. Key concepts are the *image plane* and the *aperture*

plane, the information contained within them and how interferometric measurements can be represented and understood in regard to these coordinate representations. Both of these concepts have already been touched on but will now be extrapolated to two dimensions.

The aperture plane, also called the *uv-plane* has coordinates u and v. These are the projected baseline separations in the East-West (u) and North-South (v) directions, in units of wavelength λ, which correspond to spatial frequency components. One pair of antennae, i.e. a *single* inteferometer, which produces one correlated signal, will correspond to two points in the aperture plane, namely *(u,v)* and *(-u,-v)*, of which the negative set has no physical meaning and is only a product of using the exponential form of the Fourier transformation. Each of the points in the aperture plane is associated with a discrete visibility in the image plane. By filling out the aperture plane with interferometric samples, one achieves a greater *uv-coverage*, which yields more discrete measurements of the source visibility. The amount of samples measured by an array of N antennae, is given by

$$\text{SAMPLES} = \frac{1}{2}N(N-1). \tag{35}$$

As an example, an ALMA-like array of 60 antennae will sample a total of 1770 visibility points on the sky, assuming each antennae can observe the source. The conversion between antennae position and baseline coordinates in the uv-plane follow a fairly simple matrix transformation based on declination, δ, and hour angle, H, of the phase reference point on the sky. In a general case, antenna positions are governed by X, Y *and* Z coordinates (due to the curvature of earth, the antennae are not co-planar). The coordinate system is Earth-centered with positive X values in the $(H = 0, \delta = 0)$ direction, positive Y-values in the $(H = -6^H, \delta = 0)$ direction and positive Z values in the $(\delta = 90°)$ direction. In most cases, the need for a three dimensional coordinate system vanishes, as the baseline separations between antennae are short compared to Earth's degree of curvature, but as later simulations pertain the Event Horizon Telescope - a globe spanning interferometer, the full set of coordinates are explored now. For a set of (X_1, Y_1, Z_1) and (X_2, Y_2, Z_2) coordinates for two seperate antennae, the XYZ separation in units of measured wavelength between them is $(\Delta X_\lambda, \Delta Y_\lambda, \Delta Z_\lambda)$, where each entry is simply calculated

$$\Delta X_\lambda = \frac{X_2 - X_1}{\lambda} \tag{36}$$

in the case of the X-coordinate. The corresponding (u, v, w) coordinates are calculated as (Thompson et al. [2017], eq. (4.1))

$$\begin{pmatrix} u \\ v \\ w \end{pmatrix} = \begin{pmatrix} \sin H & \cos H & 0 \\ -\sin\delta\cos H & \sin\delta\sin H & \cos\delta \\ \cos\delta\cos H & -\cos\delta\sin H & \sin\delta \end{pmatrix} \begin{pmatrix} \Delta X_\lambda \\ \Delta Y_\lambda \\ \Delta Z_\lambda \end{pmatrix} \tag{37}$$

which, as mentioned, are the projected East-West (u) and North-South (v) antenna separations, i.e. baselines, perpendicular to the source direction (w). The most common way of

representing the coverage of spatial frequencies is the (u', v')-plane, which is simply the u and v coordinates projected onto a plane, normal to the direction of the source. We define $u' = u$ and $v' = v\,\mathrm{cosec}\delta$

$$u' = \Delta X_\lambda \sin H + \Delta Y_\lambda \cos H, \tag{38}$$

$$v' = -\Delta X_\lambda \cos H + \Delta Y_\lambda \sin H + \Delta Z_\lambda \cot \delta. \tag{39}$$

An example of uv-coverage and corresponding reception pattern for a single radio dish has already been shown in Fig. 6. As already mentioned these are also called aperture-filled telescopes - there are no *gaps* in the coverage, within the extend of the aperture. In a moment, I will go through a simple interferometric observation example, but first we need to understand the *image plane*. The image plane contains two representations of the source, namely the *source intensity distribution* and the *visibility*. The intensity distribution $I(l, m)$ is the intensity as a function of position on the sky given by (l, m) angular coordinates, which are angular offsets from the reference point on the sky. This is the desired information that we wish to recover when measuring samples of the visibility, which is the two dimensional Fourier transform of the source intensity.

2.6 Observation example

I will now go through a simple observation example using the software *The Friendly Virtual Radio Interferometer* (fVRI), available from `https://crpurcell.github.io/friendlyVRI/`, written by Cormac Purcell and Roy Truelove at Macquarie University, Sydney. This specific software is very useful for illustrating the basics of interferometry and aperture synthesis, but the software does have some limitations as it ignores certain physical effects. These effects are; Multi-frequency synthesis, time-averaging of samples, non co-planar arrays (such as EHT) etc. As such, the software is useful as a "quick-look" tool, but limited for science applications. The software has two main inputs (specified in the "control window") which yield six output figures (showed in the "plotter window"). The first input is the *source model image*, as well as the source position on the sky. This is used to generate the first two figures. The unmodified model image represents the real source intensity distribution on the sky - what we are attempting to image. The Fourier transform of the model image, or *model FFT*, represents the source visibilty - what we can sample using interferometry. The second input is the *antennae configuration*, a list of antenna positions, with a reference point at the origin of the array[9]. The user must also select an *Hour Angle Range*, which corresponds to the observation time-frame. I have yet to touch on the implication of observing across a range

[9] As this software does not allow for non co-planar arrays, the Earth-centered XYZ coordinate system discussed in the prior section is substituted by a local two dimensional xy-coordinate system, but effectivly represents just the same.

of hour angles, but the advantage will become clear shortly. The antenna configuration is used to generate the remaining four figures. Firstly, the uv-coverage, calculated from the baseline separations of each pair of included antennae. The *observed FFT*, which is simply the sampled visibilities, given the uv-coverage. The *synthesized beam*, which is the collective response of each pair of antennae calculated by the Fourier transform of the uv-coverage. This is analogues to the point-spread-function, or power pattern, of a single aperture and is, in the case of radio interferometry, often called the *dirty beam*. Lastly, the *observed image*. This is the inverse Fourier transform, or Fourier synthesis, of the observed visibilites; the source intensity inferred from the measured visibility samples. Another way of explaining the final image, is that it is simply the convolution between model image and dirty beam, as also described by eq. (32). In radio interferometry, this image is often called the *dirty image* (or *dirty map*), referring to the fact that the synthesized image is corrupted by undesired data from the sidelobes of the dirty beam. Extra options include *observing frequency* and model image *pixelsize*, which controls the size of the model on the sky. Naturally smaller sources require greater resolution, i.e. longer baselines.

In this simple example, I will be using the press photo image of the HL Tauri ALMA results (`http://www.eso.org/public/images/eso1436a/`) - a protoplanetary disk ~ 450 light years away in the constellation Taurus. This image is *not* an actual physical model, but simply a .jpg image of the actual ALMA results (Brogan et al. [2015]), however the basic principles of interferometry will still be clear. The image size is 800×800 pixels and the pixelsize is set to 0.003 arcsec pr. pixel, which corresponds to an area 2.40" $\times$ 2.40" on the sky. Assuming the disk diameter is 70% of the image width, this results in an angular size of 1.68" which, at a distance of 450 light years, equates to a physical size of ~ 230 AU. The source declination is set to $\delta = 18^\circ$ to emulate the position of the actual source on the sky. The antenna configuration is the ALMA Cycle 6, Configuration C43-10 of the 12-m antennae, with baselines spanning from 250m to 16km. For this simulation I will do a *single* integration as the source passes $H = 00^{\mathrm{h}}$, observing at $\lambda \sim 1$mm (250 GHz). Results are shown in Fig. 10.

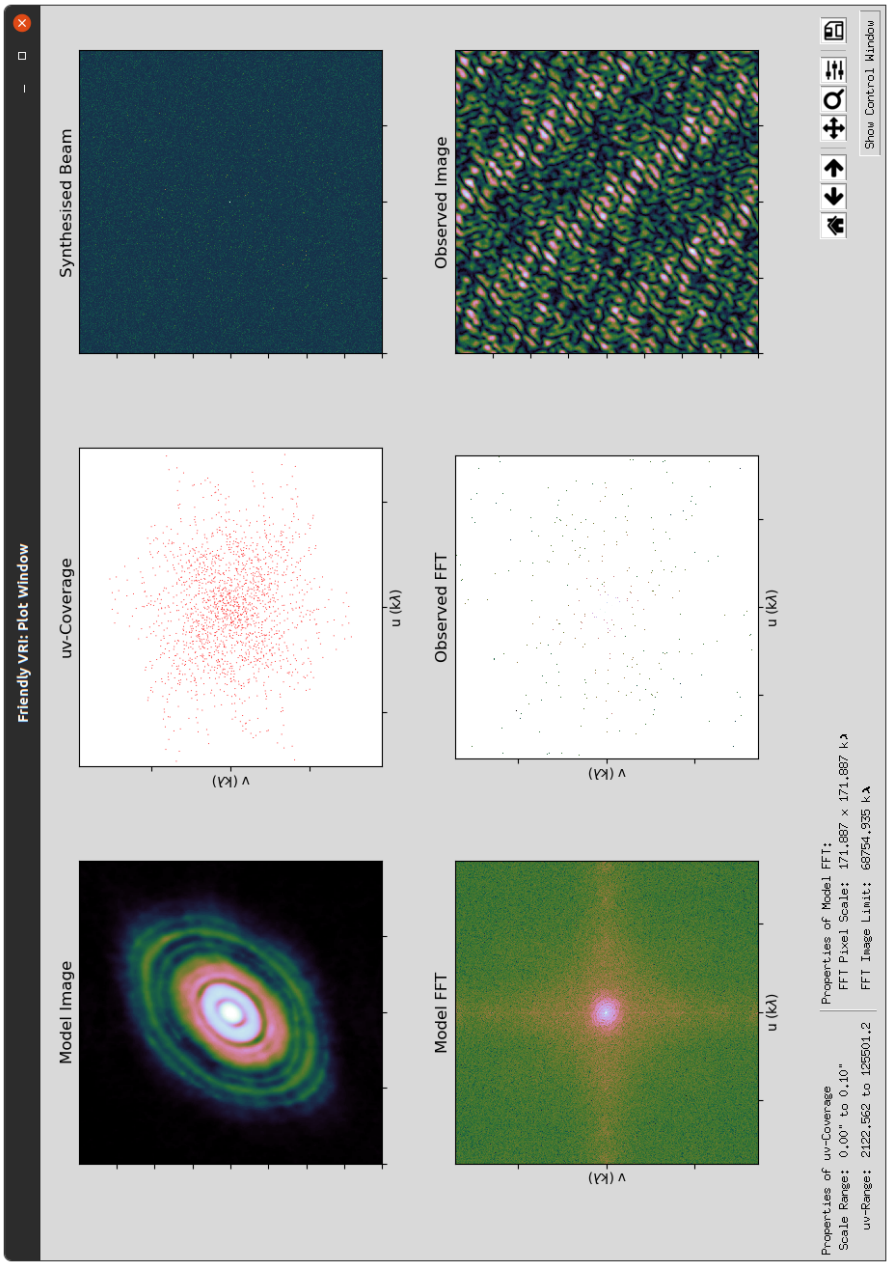

Figure 10: Output from simulated observation of HL Tauri performing a single integration at hour angle $H = 00^{\mathrm{h}}$. The first column shows model image and visibility. The second column shows uv-coverage of antenna configuration and sampled visibilities. The third column shows the array dirty beam and recovered image. The observation was done at 1 mm (250 GHz) and the source declination is $\delta = 18^{\circ}$.

From this simulation, the recovered image holds very limited information and it would be hard to make sense of it, even with knowledge of the input model. We do not have enough spatial frequency samples to obtain a good synthesized image. There is a way to gain more samples using the same array, without adding more antennae to the configuration. This is done by utilizing the rotation of the Earth, in what is known as *Earth Rotation Aperture Synthesis*. One can imagine that the projected baseline between two antennae, as viewed from a faraway source, will seem to change as the earth rotates. By measuring several samples as the source moves across the sky, each pair of antenna will effectively sample at multiple different spatial frequencies, generating *tracks* in the uv-plane. I'll run the exact same simulation as before once again, but this time we will begin the sampling of visibilities as the source passes $H = 00^{\mathrm{h}}$, however we then continue to take samples each 300s, until the source passes $H = 06^{\mathrm{h}}$. Results are shown in Fig. 11.

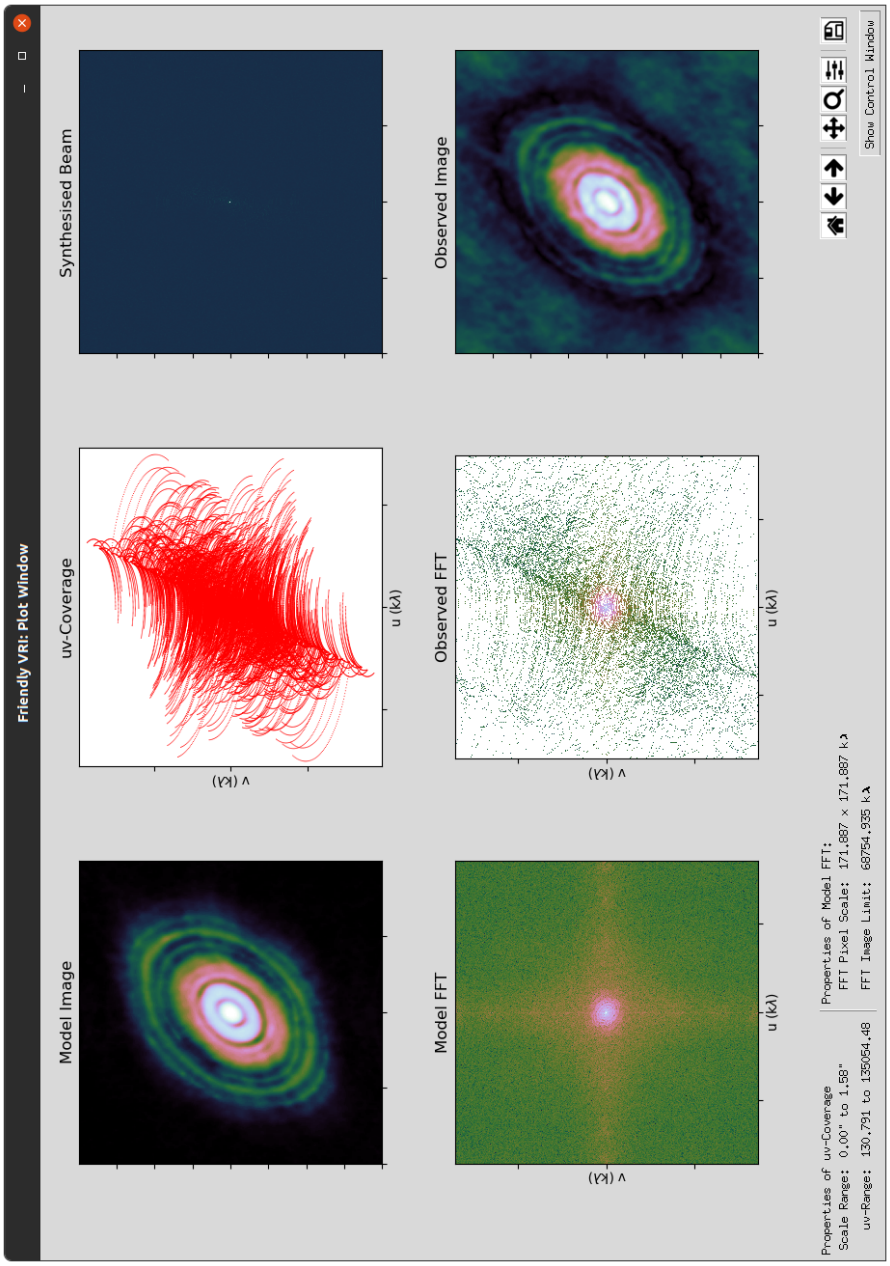

Figure 11: Output from simulated observation of HL Tauri. Observation starts when the source passes $H = 00^{\mathrm{h}}$ and ends at $H = 06^{\mathrm{h}}$, measuring each 300s. The first column shows model image and visibility. The second coloum shows uv-coverage of antenna configuration and sampled visibilities. The third column shows the array dirty beam and recovered image. The observation was done at 1 mm (250 GHz) and the source declination is $\delta = 18°$.

The recovered image is *much* better. The ring structure is visible and the central protostar is resolved. The array response seems to favor a certain orientation, as the rings are more defined in the North-South direction, but most is visible. The importance of using Earth's rotation is obvious, and most - if not all - aperture synthesis interferometers exploit this to achieve better uv-coverage, thus emulating an aperture-filled telescope to a higher degree. The largest baseline separation sets the resolution of the array, but at the very shortest baselines a problem arises. Antennae at the center of the array cannot be set infinitely close to each other and an "inner hole" in the uv-coverage will always exist for certain source sky positions. We cannot sample the shortest spatial frequencies, which correspond to large-scale emission on the sky. As a consequence, some aperture synthesis observations will intrinsically always be high-pass filtered and the low-spatial frequency data must be measured in another way, such as with a single dish telescope collecting the entire flux of the source, albeit at a comparably poor resolution.

For the configuration used in the two simple simulations described above, we have been able to achieve a fairly good uv-coverage using Earth's rotation, yet the resulting image still show discrepancies from the model image, which in large parts stem from the sidelobes of the synthesized array beam. In an attempt to clean synthesized images of unwanted sidelobe information, different algorithms have been invented and tested throughout the years and I will go through one of them, as well as how I implement it in cleaning my own simulated observations, in a later section. Beforehand, I will quickly explore some effects previously ignored, which have important implications for radio interferometry measurements, especially for very large arrays.

2.7 Data corruption and calibration

For my own simulations, I'll be working with calibrated data, which will significantly simplify the issue of imaging the observed visibilities. It can be envisioned how much work goes into calibrating the data, by looking at how the data size changes from observation to final image. In the second webinar "VLBI data series 2: Handling Data, Managing Errors" hosted by speaker Lindy Blackburn, we are informed that the data size of an EHT measurement is reduced by *12 orders of magnitude*, from the raw signals in PetaBytes, to the final image in kiloBytes. Although the observation itself is simply many measurements of a source signal, correlated between a set number of antennae, many physical factors complicate the issue greatly. This section will give a simple outline of these factors.

For very long baseline interferometry measurements, the array can no longer be approximated as co-planar and the geometric delay of measured signals are more complex to estimate due to the Earth's shape and rotation. In other words, it is difficult to know the exact relative locations and velocities of each independent station at all times, when measuring the source across the sky. This, in turn, makes the tuning of internal time

delay, i.e. delay tracking, troublesome. Relative velocities of each station also introduce dopplershifting of the measured signal, which must also be accounted for. Local station weather and atmosphere conditions introduce delays and noise which varies across the globe and corrupts the signal. Individual stations also have intrinsic thermal noises associated with them, which limits the signal to noise (S/N) ratio. Each station can also inhibit different delays related to electronics. VLBI data is not correlated immediately upon signal reception, as each station is separated by too great a distance. The observations are each recorded with time-stamps determined by an on-site atomic clock and later transported to a correlation site. Each of these clocks are independent and can be imperfect, resulting in incorrect time-stamps, and thus differences in signal reception time. In the webinar, "post-digitization" effects are also mentioned. These include any data errors that occur post recording and are especially difficult to combat, as these might not originate from any physical phenomenon. Lastly, arbitrary data issues can also arise. These include technical failure, misplaced data, human error etc. One example is sudden telescope recording failure which can happen due to issues with the receiver. Maybe the telescope pointing model is off and thus is not recording properly. Telescopic failure is not an uncommon occurrence for long inteferometric campaigns and often results in data that needs flagging after the observation. Data reduction piplelines[10] exist for several arrays and are used to best mitigate the effects of all problems mentioned above. As an example, the calibration pipeline, among other scripts and links to the relevant software *CASA*[11], for ALMA can be found at: `https://almascience.nrao.edu/processing/science-pipeline`. Calibration of data is essential, as no reliable (or sensible) information can be inferred from uncalibrated data. Luckily, for many of the most operated radio interferometers these processes are mostly automated today.

At the risk of repeating myself, it should be made clear, that even given a *perfect* calibration of the VLBI data, the necessity for cleaning algorithms, as hinted in the end of the prior section, still persists. The act of *calibrating* VLBI data and *imaging* VLBI data are different in both execution and end result. Calibration prepares the data for inspection, by correcting changes caused by physical phenomena that alter the signal from its original shape. Imaging is merely one of many ways to inspect the signal and will mostly only work if the data has been calibrated properly, depending on choice of imaging algorithm.

[10] A *pipeline* refers to a collection of steps, or tasks, working toward a final result. Each task input, is the output from the prior step. As an example, a calibration pipeline is a set of tasks that attempt to calibrate some uncalibrated input data.

[11] Common Astronomer's Software Applications.

2.8 The CLEAN algorithm

As seen in section 2.4, if the uv-coverage is good, the synthesized image does resemble the model image pretty well, albeit a bit *messy*. Naturally the problem worsens for fewer samples of the source visibility. For any sparse uv-coverage there will be missing information, i.e. the visibility samples that were *not* measured by the array. This information is lost to us and the best we can do is *guess* how the source appears on the sky, with the information that we've actually measured. On top of missing information, asymmetrical arrangements of antennae create messy and extended sidelobe patterns in the synthesized beam, that must be accounted for. There are many different ways of going about this and in this section I will explore one of them.

The most widely used imaging algorithm is CLEAN, written by Jan Högbom (Högbom [1974]). The workings of the CLEAN algorithm are, in principle, quite simple; it attempts to create a *clean map* by subtracting sidelobe disturbances continually from the dirty map. The idea can be illustrated through a simple example (Högbom [1974], section 4): Consider an observation of a point source on the sky. We know that the synthesized image, or dirty map, is simply the convolution between the dirty beam and source intensity distribution. A convolution between an arbitrary dirty beam and a point source will simply yield a dirty map equal in detail to the dirty beam[12]. At the location of maximum intensity in the dirty map, we now subtract the dirty beam pattern with equivalent intensity amplitude, which will leave an empty map. At this point a new map, the *model map* is created. Onto this map, we add a point source situated at the location of maximum intensity, with corresponding intensity amplitude. In this new map the sidelobes are gone, but so is the main beam and only a single point remains. A *clean beam* is created by fitting a two-dimensional Gaussian to the main lobe in the dirty beam and subtracting everything around it, i.e. the sidelobes. The model map is now convolved with the clean beam and the result is a *clean map*, which in theory is the recovered image, free from sidelobe disturbances. To illustrate this process, I borrow a slide from the third lecture (Jørgensen [2019]) in the course *Observational Astrophysics*[13], see Fig. 12. For a single point source, the CLEAN algorithm needs only a single iteration to clean the image. We can imagine a real observation as a collection of many points sources with varying amplitude on the sky. The algorithm will begin at the point of maximum intensity, which will be subtracted allowing for a new point of maximum intensity. In this more realistic scenario, the *empty map* from before is instead a *residual map*. Iterations continue until the value of the next maximum intensity point source is comparable to the noise level (or a set user value). When running a CLEAN algorithm, the user often has control of three primary parameters. These are *number of iterations*,

[12]Remember that the dirty beam is analogous to a point-spread-function, i.e. the response to a point source, for a standard aperture.

[13]`https://kurser.ku.dk/course/nfyk16001u/`

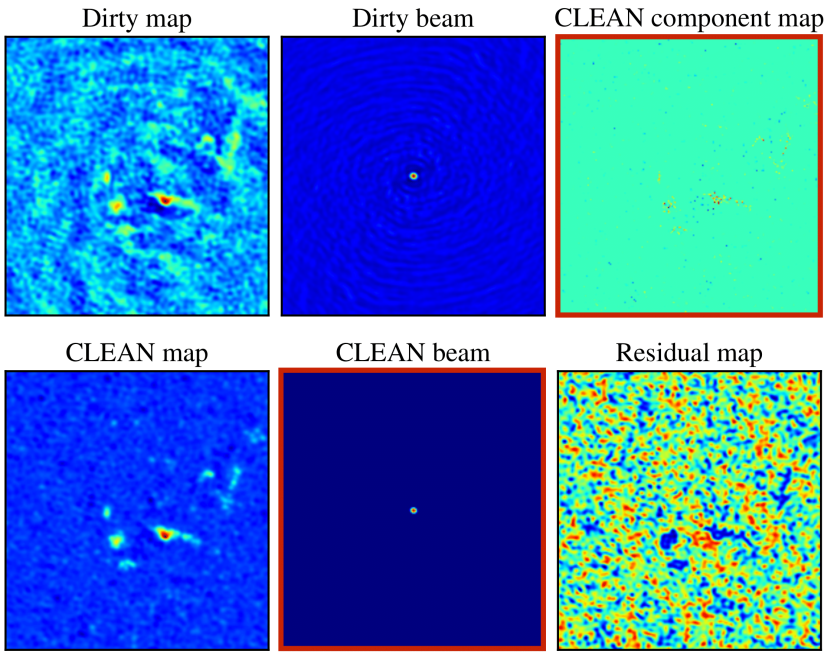

Figure 12: Example of CLEAN algorithm components. The *dirty map* represents the uncleaned data - the inverse Fourier transformed visibility samples. The *dirty beam* is the array response. The *CLEAN component map* is the model map, in which point sources are continually added as the CLEAN algorithm subtracts the dirty beam from the dirty map. The *CLEAN map* is created by convolving the *CLEAN beam* (main beam-lobe) with the CLEAN component map. The *residual map* is the leftover information in the dirty map, after the final dirty beam subtraction.

which simply controls how many iterations the algorithm will subtract and add points to the model image. The *cutoff* which sets the value of absolute intensity, beneath which the algorithm will stop itself. This is done to prevent the algorithm from cleaning beneath the measured flux level. Finally, the *loop gain*, which controls the fraction of maximum intensity that is subtracted for each iteration. Ideally, this should be small such that the amount of flux subtracted from the dirty map each iteration becomes more controlled, but low loop gain means that we require more iterations to clean effectively, which lengthens the run time. Several more options exist depending on software and my own use of the CLEAN algorithm will be examined in later sections. CLEAN is a tried and tested method and

due to its simplicity and effectiveness it also works very fast and is implemented in many different software packages (CASA, AIPS[14], DIFMAP[15], SMILI[16] etc.) used for imaging of interferometric data and is thus easily available and well-documented. The algoritm has some issues, chief among them is the necessity of calibrated data, as the clean map is solely based on the dirty map. The algorithm also has a tendency to break up features that are extended, into smaller fragments.

3 Software and array

In this section, I will present the code, software and array information that I have used to generate synthetic VLBI data. As I primarily use Windows 10 as my operating system and due to the fact that most scientific software and code operate best on Linux based operating systems, I have used the emulator software Oracle VM VirtualBox[17] to emulate Ubuntu 20.04 LTS[18] on which all the mentioned software worked flawlessly. The simulation workflow can be divided into three main steps:

1. Generating synthetic VLBI data, i.e. the interferometric samples (`eht-imaging`)
2. Cleaning and imaging the VLBI data (DIFMAP)
3. Displaying results (Python 3)

3.1 eht-imaging

The `eht-imaging` (Chael et al. [2018]) python package contains tools for simulating, imaging and analyzing in the field of radio interferometry (Documentation found at: `https://achael.github.io/eht-imaging/`). The package consists of several primary classes related to plotting, simulating, loading data, imaging etc. Each class has multiple tools within their specific function. The package is also able to produce synthesized images from visibility samples using the regularized maximum likelihood method - an alternative to the CLEAN algorithm. For my purposes, I make use of the `Image, Array` and `Obsdata` classes. The code needs two primary inputs to function. The first is the model image, which is defined using the *Image* class. As an example, an image can be loaded using the `ehtim.image.load_fits()` or `ehtim.image.load_txt()` commands. As is evident the software accepts both .fits images and .txt files as model inputs. For either type of file, source position, date and intensity are required. As mentioned, the visibility data is the two dimensional Fourier transform of

[14] Astronomical Image Processing System, found at: `http://www.aips.nrao.edu/index.shtml`
[15] Differenc Mapper, found at: `https://www.cv.nrao.edu/adass/adassVI/shepherdm.html`
[16] Sparse Modelling Imaging Library for Interferometry, found at: `https://github.com/astrosmili/smili`
[17] `https://www.virtualbox.org/`
[18] `https://ubuntu.com/download/desktop`

the model image intensity data. The specific samples that we obtain are determined by the *array*, which is loaded using the `ehtim.array.load_txt()`. The array .txt files are simply station *x,y,z* positions as well as estimated sensitivity, given the specific measured radiation (more on this in the "Array" section). Projected baseline distances are obtained from station separations and source positions, which vary as the Earth rotates. Interferometric samples are recorded with corresponding root mean square (rms) noise estimates determined by baseline sensitivity and integration time, at user defined intervals. The `image.observe()` command will initiate the observation, based on a set of user defined parameters, such as integration time, as mentioned above. My full data generation script is included in the appendix. Once the synthetic VLBI data has been generated the .uvfits file containing all data is exported for use in the imaging software DIFMAP, discussed in the next section.

3.2 DIFMAP

DIFMAP is a software developed between 1992-1995 for synthesis imaging of radio VLBI data, be it real or simulated, and is written by M.C. Shepherd of the Owens Valley Radio Observatory. The program is installed, compiled and run in a terminal. It reads and writes .uvfits files and contains several tools for inspecting, editing, calibrating and imaging. These are executed as single commands or written in script files for simple executions of larger routines. My script for cleaning the synthetic VLBI data generated by `eht-image` is attached in the appendix, but I will gloss over the main steps now. The .uvfits files are loaded into the software using commands `observe` and `select`. These load a target dataset and chooses a polarization respectively. Upon loading a dataset, the visibility samples can be inspected in a variety of ways. When I initially ran the software, it was important to check if both `eht-image` and DIFMAP agreed on measured visibilities and the uv-coverage, and that both platforms interpreted the data the same way. This was easily confirmed by comparing figures (uv-coverage and visibility amplitudes) across both software. In order to image the data, DIFMAP requires the generation of a map grid which is used to sample the dirty map and beam. These are grids of size nx and ny, and cell sizes dx and dy. I choose to work with a grid and cell size matching the resolution and pixel size of my simulation input model image, which I will discuss in a later section. Once data is loaded, visibility weighing is set (discussed in next section) and a grid has been specified, imaging can begin. As explained in the theory section, the CLEAN algorithm works by iteratively subtracting the dirty beam modified by a set loop gain and the intensity of the brightest point (or *pixel*) in the dirty map creating a residual map and delta-function model map in the process. The model map is finally convolved with the fitted (or user-defined) clean beam which forms the clean map. In DIFMAP the CLEAN algorithm operates only within CLEAN windows which are user defined. In the absence of these windows DIFMAP will itself create a square CLEAN window in the center of the dirty map, half the area of the map. For this reason I

choose a map grid of size $nx = ny = 1024$, which creates a clean map based on the central 512×512 pixels, equal in size to my input model. I will comment on pixel size and my model image in a later section. The data is occasionally phase-calibrated which allows for further subtraction of flux from the dirty map. Finally the data is phase- and amplitude calibrated before the clean map is recovered and exported. My script also exports the dirty map, dirty beam and residual map which i plot using the `Astropy.io`[19] package for Python (my plotting script is attached in the appendix).

3.3 Data weighing

When imaging visibility data it is important to consider the means by which each visibility sample is weighed, as this can significantly alter the synthesized beam and image. Depending on different weighting schemes (`https://casa.nrao.edu/Release4.1.0/doc/UserMan/UserMansu257.html`) one can achieve better performance in certain aspects of imaging, such as resolution or sensitivity. For my purposes I use two different types:

Natural weighing of visibility samples is used to enhance sensitivity, lowering noise and increasing the signal-to-noise ratio of the image. For a given sample i the image weight w_i of that sample is given as

$$w_i = \frac{1}{\sigma_k^2} \tag{40}$$

where σ_k is the rms-noise of the specific visibility sample i, thus all samples are weighed equally. I use this weighing scheme when I wish to calculate the optimum sensitivity capabilities given the set observation parameters, at the cost of slightly worse angular resolution.

Uniform weighing is used to enhance resolution of the image, at the cost of lowering sensitivity and signal-to-noise ratio. Effectively the visibility sample weight is calculated the same way as for the *natural* scheme, but typically with errors raised only to the power of -1. The data is then re-weighed inversely to the number of samples within a set bin-size which favors regions with dense uv-coverage. This suppresses the side-lobes and amplifies the main-lobe at the cost of increased noise in the field of view. I favor this weighing scheme when presenting synthesized images as the resolution quality is enhanced. Examples of beams produced using both of these weighting schemes as well as estimated image rms-noise are shown in Fig. 13. The rms-noise is lowered by $\sim 62\%$ by changing the weighing scheme but at a great loss of a defined main lobe, which shows the significance of choosing proper weights when producing an image. There exist many other types of weights such as the *Briggs* scheme in which the natural and uniform scheme is combined by som mixing parameter, such that the user can tune a balance between sensitivity and resolution, a type of convolution of the two beams above.

[19] `https://www.astropy.org/`

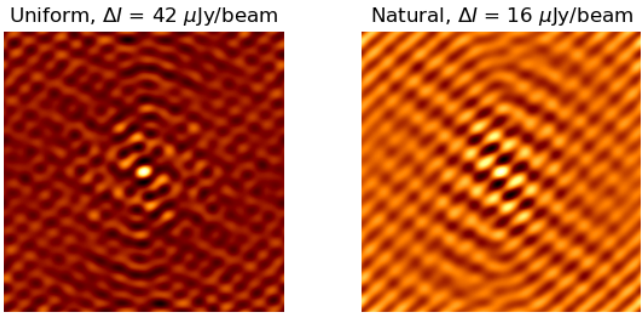

Figure 13: Synthesized beam after 9 hour campaign using the current Event Horizon Telescope with GLT located at Thule. Left image shows beam produced using uniform visibility data weighing; right image shows the same for natural data weighing.

Specifics regarding DIFMAP settings to enable these weighing schemes have been located in the DIFMAP manual, as well as the offical cleaning script used in cleaning the 2017 M87* data, located on github (`https://github.com/eventhorizontelescope/2019-D01-02`) which was also compared to another "deep-clean" script by Dan Homan (`http://personal.denison.edu/~homand/final_clean_rms`).

3.4 Array

To construct my .txt array file, I used an online geodetic-to-cartesian converter APSalin[20]. My chosen reference ellipsoid is the "World Geodetic System 1984" (WGS84). Geodetic coordinates for each of the 12 sites (summit included) were found in their respective Wikipedia articles (geotags) and converted to cartesian coordinates using APSalin. WGS84 cartesian coordinates are shown in Table 1. Comparing my derived locations to the documented locations on the EHT website, show that they mostly agree down to a few kilometers. The biggest deviator is the South Pole Telescope (SPT), but this telescope will not be included in my simulations, as it is not available for observations of M87*[21]. The choice of constructing my own array, instead of merely using information already available on the website, is driven by the fact that I want to ensure that my derived location for the Summit Camp is defined within a coordinate system in which each telescope location is based on the same reference.

System equivalent flux densities (SEFD) for each station were found on the Event Horizon

[20] `http://www.apsalin.com/convert-geodetic-to-cartesian.aspx`

[21] In the 2017 observation of M87*, the South Pole Telescope was used to observe calibration source 3C279.

Site	X[m]	Y[m]	Z[m]
ALMA	2225015.31	-5440016.42	-2481631.27
APEX	2254114.67	-5429390.67	-2478926.05
JCMT	-5464560.74	-2492993.49	2150640.51
SMA	-5464542.71	-2492870.04	2150792.76
LMT	-768714.93	-5988549.54	2063376.21
IRAM 30m	5088910.37	-301688.02	3824972.34
SMT	-1828803.67	-5054427.64	3427879.39
SPT	0	0	-6359552.31
NOEMA	4523926.85	468134.39	4460280.92
KP	-1994313.74	-5037909.27	3357618.62
GLT (Thule)	541287.15	-1388548.57	6180864.19
GLT (Summit)	1500561.35	-1191856.16	6066429.12

Table 1: WGS84 Cartesian coordinates of 11 concurrent stations in the Event Horizon Telescope network. Positions are inferred using Wikipedia article coordinates for each station, subsequently converted using the online tool APSalin.

Telescope website[22] and are displayed in Table 2. The SEFD is analogues to telescope sensitivity and is defined as the source flux density that doubles the system temperature. Therefore a *lower* SEFD is indicative of more sensitive equipment.

Distance as well as estimated 230GHz / 345GHz resolution - using equation (1) - are listed in Table 3. Colors are indicative of arbitrary sensitivity classification. In this chart GLT remains at Thule, the following section will cover the relocation in more depth.

[22] `https://eventhorizontelescope.org/for-astronomers/proposals`

Site	SEFD [Jy]
ALMA	74
APEX	4700
JCMT	10500
SMA	6200
LMT	1000
IRAM 30m	1900
SMT	17100
SPT	19300
GLT	4127*
NOEMA	700
KP	13000

Table 2: System equivalent flux densities for each concurrent node in the Event Horizon Telescope network as of 2021. Values are from the Event Horizon Telescope webiste: `https://eventhorizontelescope.org/for-astronomers/proposals` under the "Techincal Information" tab.
*The value for The Greenland Telescope differs slightly from the website and is estimated from my own calculation in the following section.

Site	ALMA	APEX	JCMT	SMA	LMT	30m	SMT	SPT	GLT	NO	KP
ALMA		31	9448	9449	5467	8624	7177	7041	9710	9401	7215
APEX	>1000		9467	9468	5485	8606	7190	7044	9708	9385	7230
JCMT	24 / 16	24 / 16		<1	5855	10908	4627	10416	7317	10671	4469
SMA	24 / 16	24 / 16	>500		5854	10908	4627	10416	7316	10671	4469
LMT	42 / 27	42 / 28	39 / 26	39 / 26		8352	1964	10363	6311	8686	2020
30m	27 / 18	27 / 18	21 / 14	21 / 14	28 / 18		8402	11389	5236	1147	8534
SMT	32 / 21	32 / 21	50 / 33	50 / 33	118 / 77	28 / 18		11166	5161	8481	181
SPT	33 / 22	33 / 22	22 / 15	22 / 15	22 / 15	20 / 13	21 / 14		12629	11737	11126
GLT	24 / 16	24 / 16	32 / 21	32 / 21	37 / 24	44 / 29	45 / 29	18 / 12		4719	5265
NO	25 / 16	25 / 16	22 / 14	22 / 14	27 / 17	202 / 132	27 / 18	20 / 13	49 / 32		8603
KP	32 / 21	32 / 21	52 / 34	52 / 34	114 / 75	27 / 18	>500	21 / 14	44 / 29	27 / 18	

Table 3: **Above diagonal:** Baseline Distance [km] for site-pairs. **Below diagonal:** Estimated 230GHz / 350GHz resolution [μas] of site-pairs. Color indicates arbitrary sensitivity classification; *Green* represents pairs with both stations having < 3000 Jy SEFD's, *Yellow* Represents pairs where one station has < 3000 Jy, *Red* represents pairs with both stations having > 10000 Jy. SEFD is estimated with respect to 230GHz receiver system temperature.

While the $\sim$ 13000 km baseline that spans between the Greenland Telescope and the South Pole Telescope seems promising for high resolution interferometric sampling, one should note that these two observatories are nearly anitpodal points on Earth and thus share precious little sky coverage, not to mention that each station exhibits medium SEFD values at 230GHz. While not impossible, the correlation of data between GLT and SPT is very limited by source position on the sky. More prominent is the baseline spanning between GLT and ALMA, as this is both governed by the high sensitivity of ALMA as well as plenty or shared sky, which holds true for both the Thule and Summit placement of GLT.

4 Relocation of the Greenland Telescope

At the time of writing, the Greenland Telescope is operating close to the Thule Air Base, Northwestern Greenland, near sea level at an altitude of approximately 70 meters. Precipitable water vapour (PWV) values greatly hinder the capabilities of the 345GHz receivers on the telescope, but allow for medium to good atmospheric transmission at lower frequencies $\sim$ 230GHz. On-site PWV and opacity values are not measured continuously, thus I had to contact the people involved with GLT to acquire estimates.

4.1 230 GHz Opacity

In 2016 Satoki Matsushita performed a study on the 225Ghz opacity at the proposed new site, the Summit Camp, central Greenland (Matsushita et al. [2016]). He is currently working on a similar study of the atmospheric data measured in Thule and generously supplied me with the most recent estimates for both sites (S. Matsushita, priv. comm). These are summed up in table 4.

	Thule	-	Summit	-
Percentile	Winter	Summer	Winter	Summer
25%	0.13	0.24	0.0464	0.0885
50%	0.17	0.33	0.0602	0.1178
75%	0.21	0.44	0.0801	0.1586

Table 4: Yearly 225GHz opacity values for the current GLT site, near Thule Air Base, and for the proposed new site, the Summit Camp. Summit values from Matsushita et al. [2016] and Thule values from Dr. Satoki Matsushita, priv. comm.

Furthermore, I was also in contact with GLT lead scientist Nimesh Patel who informed me that 225GHz Thule opacities usually exhibit values around $\tau \sim 0.5$ while excellent

conditions can lower this to around 0.1-0.2, which agrees with values given by Matsushita. For a given opacity, one can relate

$$\tau = -\ln(T) \tag{41}$$

where T is the atmospheric transmission. I will convert between opacity and transmission to illustrate atmospheric conditions more clearly. At the Thule site during Winter season (Nov. - April), measurements indicate atmospheric transmission of 88% or better, 25% of the time. Median values suggest transmission at around 84% while most measurements, about 75%, indicate transmissions above 81%. Measurements at the Summit Camp indicate that excellent winter conditions (25th percentile) will allow for transmission upwards up 95%, which is nearly loss-less transmission. Median value indicates continually excellent transmission at around 94% with typical values only lowering this estimate to 92%. These values suggest a typical (75th percentile) 225GHz transmission increase of around $\sim 14\%$ (opacity decrease of around $\sim 62\%$), during Winter, which is quite significant. For Summer seasons typical transmission increase is $\sim 33\%$ (opacity decrease of 64%). Another significant improvement is the yearly variation in atmospheric transmission. For typical (75th percentile) values, the Thule site will exhibit yearly atmospheric transmission values of 81-64% (Winter-Summer), while the corresponding Summit Camp estimates are much more generous at 93-85%. In other words, the Summit Camp is typically estimated to exhibit higher atmospheric transmission during *Summer* than Thule during *Winter*. The Summit Camp will undeniable be governed by not only better atmospheric transmission, but also year-round performance, which can be attributed to the several kilometer increase in altitude.

4.2 345 GHz Opacity

345GHz opacity measurements for the Thule site are currently not available, thus I must take an alternate approach to estimate these values. The 345 GHz receiver on the Greenland Telescope could prove to be an important part of high frequency EHT campaigns, but is currently hampered by PWV content above the Thule site. In order to estimate the PWV values I make use of ATRAN[23], an online synthetic transmission spectra solution calculator. Using known atmospheric 230 GHz transmission values for the Thule site, as discussed in the previous section, I can estimate the expected atmospheric PWV values that will match the known opacity. I use an observatory altitude of 230 feet ($\sim$ 70m), closest observatory latitude of 59° and an average zenith observation angle of 45° and Fig. 14 shows the best solutions I obtained. I have chosen to show all three solutions for each winter (W) percentile value, but only the most typical (75th percentile) summer (S) solution to keep the figure from being overpopulated. The two vertical lines indicate receiver wavelengths, i.e. 345 GHz (0.86 mm) and 225 GHz (1.3 mm) and the squares are corresponding transmission

[23]https://atran.arc.nasa.gov/cgi-bin/atran/atran.cgi

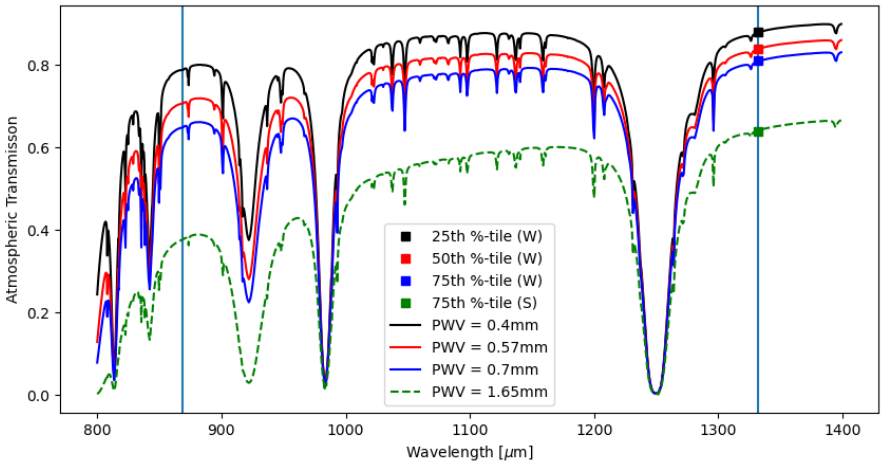

Figure 14: ATRAN transmission spectra solutions for Thule 225 GHz opacity values during winter and summer seasons, for 45° source positions. Squares indicate known values and vertical lines are relevant receiver wavelengths (345GHz and 225GHz).

values from Table 4. I estimate typical (75th percentile) Winter PWV values at Thule to be $\sim$ 0.7mm, while typical Summer PWV values increase to $\sim$ 1.65mm. During excellent conditions, I estimate the precipitable water vapour content to reach as low as $\sim$ 0.4mm. Utilizing these solutions, I can extrapolate 345 GHz transmission and convert to opacity. For typical winter conditions, I estimate a 345 GHz transmission of $\sim$ 65%, almost half of the incoming radiation is absorbed in the atmosphere. Typical summer conditions greatly worsen this, lowering transmission to $\sim$ 38%. Corresponding opacities are respectively 0.430 during Winter and 0.967 during Summer. Based on these estimates I conclude that the current 345 GHz receiver capabilities range from medium to poor, for GLT located at Thule.

Matsushita et al. [2016] derive a linear correlation between the 225 GHz opacity and higher frequency atmospheric opacity windows at the Summit Camp, given as

$$\tau_\nu = \tau_{225\mathrm{GHz}} \times \alpha_\nu + \beta_\nu \tag{42}$$

where α_ν and β_ν are coefficients that are frequency dependant. These are listed in Matsushita et al. [2016], Table 3. For $\nu = 345$ GHz they find $\alpha = 3.80$ and $\beta = -0.032$. Using the 75th percentile 225 GHz opacity value of 0.0801 (during winter), I can then estimate a typical 345GHz opacity at the Summit Camp of 0.272, corresponding to an atmospheric transmission of 76%. During summer, corresponding values increase to an opacity of 0.565,

or an atmospheric transmission of 57%. Typical 345 GHz opacity values are summarized in Table 5.

	Thule	-	Summit	-
Percentile	Winter	Summer	Winter	Summer
75%	0.430	0.967	0.272	0.565

Table 5: Estimated typical 345 GHz opacities for both GLT sites. Thule values estimated from ATRAN solutions matched to data from Dr. Satoki Matsushita, priv. comm. Summit values estimated from linear relation from Matsushita et al. [2016].

While the 345 GHz opacity estimates at the proposed Summit Site are not excellent, they are significantly better than the Thule values, especially during the summer season. I estimate a potential increase in 345 GHz transmission of $\sim 17\%$ (opacity decrease of 37%) during winter and $\sim 50\%$ (opacity decrease of 42%) during summer, following the relocation to the Summit Camp. This will significantly widen the otherwise limited use of the 345 GHz receiver on the telescope.

4.3 GLT System temperature

Dr. Satoki Matsushita also kindly provided me with information regarding typical aperture efficiencies, η_a, as well as typical system noise temperatures, $T_{\rm sys}$, when operating GLT both at Thule as well as the estimated Summit values. These, and the expected system equivalent flux density (eq. from The EHT Collaboration et al. [2019b], Table 3)

$$\mathrm{SEFD} = \frac{2\mathrm{k_B}\mathrm{T_{sys}}}{\eta_\mathrm{A}\mathrm{A_{geo}}} \tag{43}$$

are shown in Table 6.

The Greenland Telescope Project aims to move GLT $\sim$ 1000km south-east and up to an altitude of around 3km above sea level. To summarize thus far, the relocation will significantly improve the performance of GLT's high frequency 345 GHz receiver, while also slightly improving the 230 GHz receiver used in the first ever image of the M87 supermassive black hole. While the telescope will be relocated a long way from Thule, baselines spanning between other EHT sites will remain largely the same. As an example the ALMA-GLT baseline will change from 9710km to 9573km, thus the baseline will continue to function as a high resolution interferometric sampler. Judging from values in Table 6, one should not expect any significant improvement in 230 GHz observations following the relocation. While the 230 GHz receiver sensitivity will increase by $\sim 13\%$ one should keep in mind that the collecting area of GLT is only a very small part of the total synthesized dish-area of

Thule Air Base	230GHz	350GHz	650GHz	850 GHz
η_A	0.71	0.61	-	-
T_{sys} [K]	120	350	-	-
SEFD [Jy]	4127	14009	-	-
Summit Camp	230 GHz	350 GHz	650 GHz	850 GHz
η_A	0.71	0.61	0.32	0.17
T_{sys} [K]	105	200	960	1550
SEFD [Jy]	3611 ($\downarrow$ 12.5%)	8005 ($\downarrow$ 42.8%)	73309	222609

Table 6: Estimated aperture effeciency, system temperature and system equivalent flux density (SEFD) for recievers on the Greenland Telescope at both the Thule Air Base (grey) and Summit Camp (blue) sites. Red entries are missing due to site limitations (Dr. Satoki Matsushita, priv. comm.).

EHT. The primary gain of the Summit site is the improved typical weather conditions that allow for more effective use of higher frequency receivers, which in turn should allow for improved S/N ratio in high resolution observations at lower wavelengths ($\leq$ 1mm). For a single baseline, this can be estimated as (The EHT Collaboration et al. [2019b], p. 5)

$$\mathrm{S/N}_{1,2} = \frac{\eta_Q \sqrt{2\Delta\nu \mathrm{T}_{\mathrm{int}}} \mathrm{S}_{\mathrm{cor}}}{\sqrt{\mathrm{SEFD}_1 \mathrm{SEFD}_2}} \tag{44}$$

where η_Q is the digital loss due to sampling at each antenna, $\Delta\nu$ is the bandwidth size, T_{int} is the on source integration time and S_{cor} is the expected correlated flux on the baseline. Using the ALMA Cycle 7 Technical Handbook (Remijan et al. [2019]), Fig. 4.23, I make a simple estimate of the ALMA band 7 SEFD using $T_{sys} \sim 170$K, which gives $\sim$ 166 Jy, such that S/N ratios for 230 GHz and 345 GHz observations on the ALMA-GLT baseline can be estimated. These are shown in Fig. 15. I use $\eta_Q = 0.88$ (The EHT Collaboration et al. [2019b], p. 5), $S_{\mathrm{cor,230GHz}} = 0.8$ Jy and $S_{\mathrm{cor,345Hz}} = 0.03$ Jy. Estimated correlated flux values are approximated from DIFMAP visibility inspection tool `vplot`.

While $>$ 10 S/N ratios are achieved fairly quickly ($<$ 1s) during 230 GHz observations, the overall improvement due to the GLT relocation is expectantly small. For 345 GHz observation the improvement is more noticeable, but achievable S/N ratios are significantly lowered due to increased baseline uv-distance, which lowers measured visibility amplitudes. Corresponding plots for the remaining GLT baselines are shown in a later section.

5 VLBI simulations of M87* model

In this section, I will present my simulated VLBI observations of the supermassive black hole at the centre of Messier 87. I will probe the importance of the Greenland Telescope's

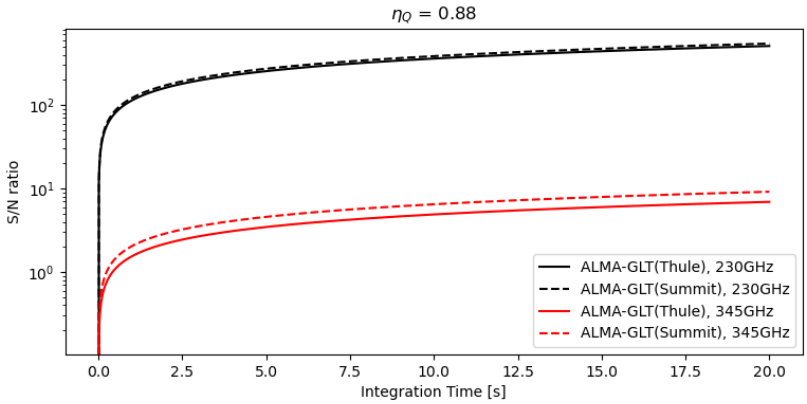

Figure 15: Estimated S/N ratio as function of integration time in seconds for the ALMA-GLT baselines for both 230 and 345 GHz observations. Results are produced assuming a measured correlated target flux of 0.8 Jy for 230 GHz, 0.03 Jy for 345 GHz and correlator efficiency $\eta_Q = 0.88$

relocation to the summit camp, as well as its inclusion in the network in general. Each simulated observation will be subject to random thermal errors as dictated by the SEFD by each site. Due to these random effects, I will present what a typical observation may look like, but I will later present some statistics based on 50 simulated observations, for each relevant configuration (200 in total).

Prior to the simulation results, I will touch on the physical conditions that are thought to generate the observed emission from supermassive black holes (SMBHs) and M87* in particular.

5.1 SMBH emission mechanisms

M87 is a giant elliptical galaxy in the local universe, situated in the Virgo cluster, with redshift $z \approx 0.004$[24]. Extending from the galaxy is a *jet* that spans several kpc, which emits radiation from radio through to γ-rays. This jet was originally observed in 1918 (Curtis [1918]) and was later found to originate from a central core of mass $\sim 6.2 \times 10^9 M_\odot$ (Gebhardt et al. [2011]). Although the exact specifications of the core-object in M87 (and other galaxies alike) remain somewhat elusive, generally accepted models expect the central region to contain a supermassive black hole surrounded by an optically thin accreting disk of hot magnetized plasma that is heated through energy gain during viscous infall. As such, expected dominant radiative processes are synchrotron emission and bremsstrahlung, modified by Compton scattering (Yuan and Narayan [2014], section 2.4). Resulting spectra

[24]From the NASA/IPAC Extra-galactic Database (`https://ned.ipac.caltech.edu/`)

are products of many parameters such as black hole (BH) mass, accretion rate, electron density and temperature. Depending on the accretion rate the spectrum will exhibit an initial peak at the lower frequencies. Radiation up to this first peak is thought to arise from synchrotron radiation from thermal electrons, which produce a wide range of photons, including radio emission. Radiation at the peak is believed to originate from the gas near the black hole, while lower frequencies originate from larger radii. Higher frequency radiation is believed to stem from comptonized synchrotron photons which are up-scattered to the X-ray / γ-ray region. The intensity of this region is closely related to the mass accretion rate $\dot{M}$ and will, for high values of $\dot{M}$, dominate the spectrum, while on the contrary, synchrotron emission will dominate for lower values of $\dot{M}$. One other source of γ-rays could be proton-proton collisions in the surrounding plasma, which can create pions that subsequently decay. For particularly low values of $\dot{M}$, X-ray emission is dominated by thermal bremsstrahlung (free-free) emission from the optically thin hot ionized accretion flow. At larger radii, it is believed that there may exist an optically thick thermal disk that emits a multi-colour (varying temperature) blackbody radiation spectrum, which further modifies the Compton spectrum by supplying lower energy photons. X-ray irradiance of the upper parts of the outer thermal disk is believed to generate emission lines that can be used to infer constraints on gas density and outflow parameters.

Works on modeling the spectral energy distribution (SED) [Prieto et al. [2015] & Broderick and Loeb [2009]] of the M87 core describe the emission as the sum of radiation from both the jet and the disk, aptly named the "jet-disk" model. Relevant frequencies for this work are in particular 230 GHz and 345 GHz radiation. Both articles conclude that the M87 SED exhibits a flat radio spectrum with flux densities around ~ 1 Jy for both relevant frequencies. These values are corroborated by photometry data from the NASA/IPAC extragalactic database, reporting 1.31 Jy and 1.51 Jy for observed 1 mm and 229 GHz passbands respectively. The fraction of total flux density supplied by each component varies for the two articles, but both agree that radio emission predominantly originates from synchrotron emission in the jet. At the time of writing, no consensus for jet formation is currently in place. More specifically, it is unknown exactly *where* the jet is formed, but the general belief is that it is very near the BH horizon. It is for this reason that radio measurements of SMBHs are of such importance in revealing the nature of these outflows.

5.2 M87* model and observational VLBI parameters

The model image I use for my simulated observations is included with the `eht-imaging` package and is called *howes_m87.txt*, see Fig. 16. More information on the origin of the model can be found in Chael et al. [2019]. This raster image is a snapshot of the 230 GHz flux density from an object consistent with the supermassive black hole, centered in M87. The total flux density of the image is ~ 1 Jy, which agrees with observations

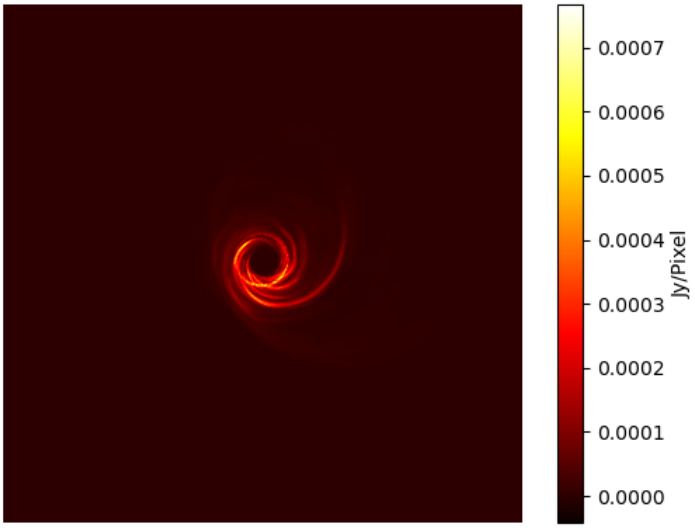

Figure 16: Model Image *howes_m87.txt* present in the `ehtim` package. The image is a 512×512 raster image showing the output of a simulation of the supermassive black hole shadow at the center of Messier 87, $M87^*$. Total image flux is $\sim$ 1 Jy and pixel-size is 0.7 μas/pixel, corresponding to an image FOV that is almost $370 \times 370 \mu$as.

reported in Broderick and Loeb [2009], Figure 2 and Prieto et al. [2015], Figure 3. I choose to use the same total flux density for both the 230 GHz model and the 345 GHz model, due to the estimated flat radio spectrum of the source. Furthermore, I assume that both radiation frequencies are emitted from the same region, which allows me to use the same model for both frequency bands, altering only the rest emission frequency between simulated observations. The model image can be convolved with a circular Gaussian beam representing the achievable resolution at different array observation frequencies to generate what an optimal clean image should look like. This is also referred to as a *blurred* model image. This is ideally what we should observe, given a filled uv-coverage and good S/N values. Blurred model images for theoretical 230 GHz, 345 GHz and 650 GHz resolutions are shown in Fig. 17 For this particular model, the central depression is only slightly visible at $\theta = 20\mu$as and only becomes well defined for resolutions $\theta > 20\mu$as. For convenience, I restore my produced DIFMAP CLEAN models with circular beams of appropriate size compared to the receiver frequency and equal to the resolutions seen in Fig. 17. The observed flux from

Figure 17: Blurred model images of M87* model, observed at 230 GHz, 345 GHz and 650 GHz. Resolution increases for higher observed frequencies, which yields a sharper image. Further increase in observing frequency will yield a blurred model image which closely resembles the original model image.

the supermassive black hole is the sum of radiation stemming from both the accretion disk as well as the produced jet. As mentioned, the radio flux is thought to be predominantly generated by synchrotron emission in the (magnetically dominated) jet, and not the disk. For this reason, it is believed that for 230 GHz and 345 GHz radiation, particular details regarding disk emission are less likely to play any import role in the produced image. From Prieto et al. [2015], section 3.2 they report a spectral index $\alpha \sim 3$ for the disk, i.e. $F_\nu \propto \nu^{-3}$, which would dictate a difference in contributed flux from the disk at 230GHz and 345GHz of

$$\frac{\mathrm{F}_{\nu,345\mathrm{GHz}}}{\mathrm{F}_{\nu,230\mathrm{GHz}}} = \left(\frac{345\mathrm{GHz}}{230\mathrm{GHz}}\right)^{-3} \approx 0.3. \tag{45}$$

This implies that for any particular disk flux density at 230GHz, its contribution is significantly lowered, by $\sim \frac{2}{3}$, when measuring 345GHz radiation instead, allowing for a more unperturbed image of the jet alone.

The model image pixel size is $\sim 2 \times 10^{-10}$ degrees, or $\sim 0.72\mu$as, which results in an image that is 367μas across. In my simulations, I slightly magnify the image such that the pixel size is $\sim 1.39 \times 10^{-10}$ degrees, or 0.5 μas, resulting in an image that is ~ 256 μas across. For each frequency band, I will present three different simulated observations using different configurations:

1. The 2020 Event Horizon Telescope configuration, *excluding* the Greenland Telescope
2. The 2020 EHT configuration, *including* GLT located at Thule
3. The 2020 EHT configuration, *including* GLT located at the Summit Camp

All simulated observations will share global parameters, namely campaign time, time between scans, receiver bandwidth size and integration time. My parameters are inspired by

the campaign schedule and information presented in the second EHT/M87 paper (The EHT Collaboration et al. [2019b], figure 12). For all my simulations I choose to observe on April 1st, 2017 (MJD: 57844), to replicate the sky position of M87 and resulting uv-coverage of the real observation. Scans initiate at 01^{h} UTC (Universal Time) and end at 09^{h}, with 300s (5min) scans occurring every 1200s (20min). That is a total of 24 possible scans pr. baseline, given that M87* is in view throughout the entire campaign. Thermal noise is included in the simulation. In total, the source flux is integrated for 120 minutes, or 2 hours. Following my simulated observations, any baseline detection with achieved S/N ratio < 3 are flagged, i.e. excluded when imaging the data. This is done to limit inclusion of data that is mostly noise.

The second 2019 paper on the first image of M87* show the aggregate baseline coverage of the M87* observations in 2017 (The EHT Collaboration et al. [2019b], Fig.11), displayed in Fig. 18.

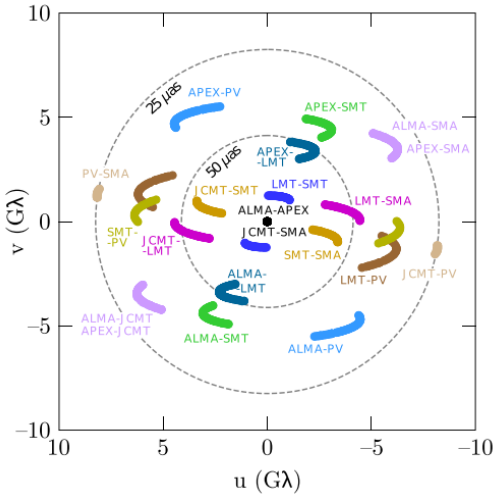

Figure 18: Baseline coverage of 2017 M87* observation. Figure obtained from The EHT Collaboration et al. [2019b], Fig. 11. Included telescopes are ALMA, APEX, JCMT, LMT, PV30m, SMA and SMT.

I test that my simulation software returns a similar baseline coverage, by running a simulation using the 2017 EHT configuration (same as Table 1, excluding GLT, NOEMA and the KP12m telescope) and my observational parameters described above. Fig. 19 shows the result. Based on the similarity of the produced uv-tracks, I can confirm that my observational parameters replicate source sky position and observing time well. Adding new telescopes to the simulation will thereby constrain them to similar conditions of the actual observation in 2017. Atmospheric fluctuations above each site results in phase-corruption of the incoming signal on timescales that are much shorter (< 10s) than minute-long integration times.

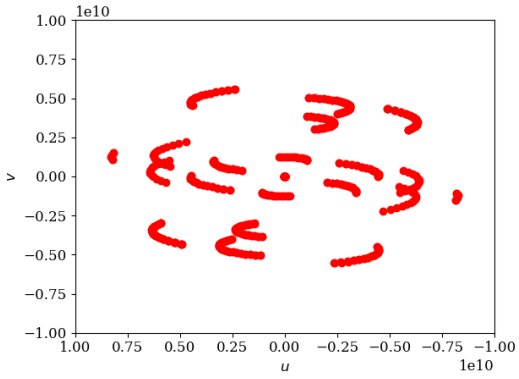

Figure 19: Baseline coverage from simulated M87* observation using observational parameters described above.

This should in practice disallow integration times exceeding these timescales. For real observations, integration times exceeding atmospheric coherence timescales are achieved using a two-stage approach as described in The EHT Collaboration et al. [2019b], section 2.2: Firstly, detections are achieved within atmospheric coherence timescales on high sensitivity ALMA baselines (see Fig. 15), which are used to calculate phase calibration solutions. Secondly, these phase calibrations are applied to non-ALMA baselines, correcting for atmospheric turbulence, allowing for integration times of many minutes. In my simulations, this effect is replicated by removing time dependant station-based random phases and gains, effectively calibrating the signal before reception, allowing for long integration times.

In reality the total observation campaign would likely be divided into scans of not only the source, but bandpass, flux and phase calibrator sources as well, used in calibrating the array in between source integration. In my simulations, only the source is observed and the data is calibrated in-code using `eht-imaging` and subsequently imaged using the CLEAN algorithm in DIFMAP utilizing uniform weighing of the visibility data, for enhanced resolution. All output .fits files are displayed using `matplotlib.pyplot` and `astropy`. The output of the simulation is Jy / beam, which is converted to brightness temperature using

$$T_b(I) = 1.36 \frac{\lambda^2}{\theta_{maj}\theta_{min}} I \tag{46}$$

with λ being the observed wavelength in cm, minor and major beam widths are θ in arcseconds and I is the output in mJy / beam. The equation comes from the Rayleigh Jean's law (see `https://science.nrao.edu/facilities/vla/proposing/TBconv`).

It is important to acknowledge that the physical model is prone to uncertainty as the radiative processes from hot accretion flows, as well as the created outflows, are as of yet still poorly understood. Returning to the aforementioned results of Prieto et al. [2015] and Broderick and Loeb [2009] they both agree on a flat $\sim$ 1 Jy jet-emission dominated

radio spectrum up to $\lambda \sim 1$mm, followed by a power-law decrease, which is indicative of a slowly accreting black hole. The two articles do not agree about the disk emission peak and contribution to total flux density. Broderick and Loeb [2009] states that the SED is disk dominated for emission > 7 mm, with disk peak emission somewhere > 10 mm. At around 1.3 mm they state that a slight contribution to the total flux stems from the disc (about 5%), while at $870\mu m$ the flux is $\sim \frac{1}{100} F_{\nu,\mathrm{Jet}}$. Their SED modelling work from the cited article is shown in Fig. 20.

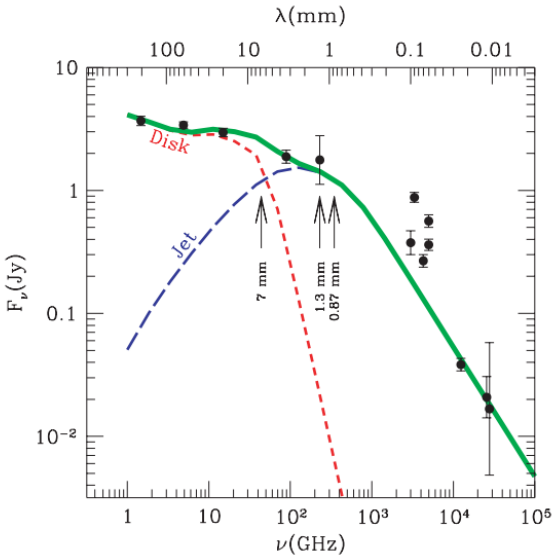

Figure 20: Jet-disk model from Broderick and Loeb [2009]. Dashed lines show individual component contribution to the total flux density, shown by the solid green line. Data points represent samples measured between 1991-2008.

At 1.3 mm and 870 μmm the total flux density is almost completely dominated by jet emission, which peaks at around ~ 2 mm. The work by Prieto et al. [2015] proposes a disk emission which peaks at around ~ 10 μm with lower contribution to total flux density at around $\sim 0.01\%$ for 1.3 mm and 0.87 mm. Their modelling work is shown in Fig. 21. In contrast to the prior SED, the disk emission spectrum incline is inverted due to the shift in estimated peak position, from $> 10\mathrm{mm} \rightarrow 10\mu$m, thus for a given disc flux density contribution at 230 GHz they propose an increased contribution at 345 GHz implying a slightly disc-perturbed view of the jet emission. While both works agree on the general shape and expected flux density, especially from the jet, the expected peak emission and flux density scaling for the disk remains a point of contention. Physical model uncertainty is an important consideration when interpreting the simulated observations. Most likely,

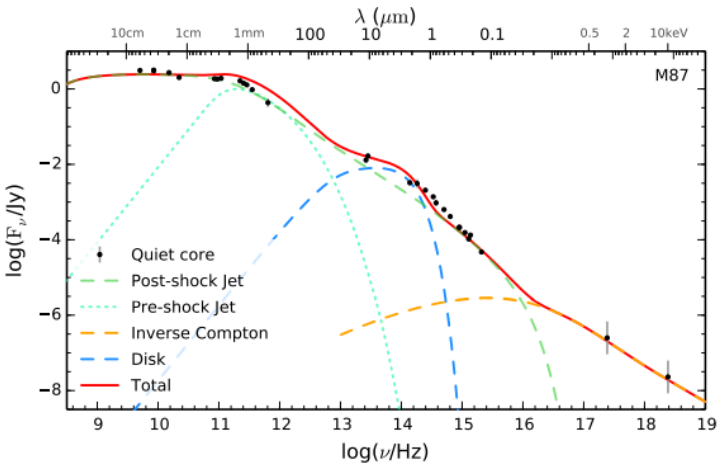

Figure 21: Jet-disc model from Prieto et al. [2015]. Dashed lines show individual component contributions which sum to the total, solid red, estimated flux density. Data points are Chandra X-ray measurements.

when observing at 230 GHz and 345 GHz, we will predominantly observe synchrotron radiation stemming from the jet and quite possibly a very small bremsstrahlung or blackbody contribution from the disc. Depending on which work one chooses to believe, the difference in measuring 230 GHz and 345 GHz, aside from increased beam resolution, is that the 345 GHz observing band might limit the amount of radiation captured from the disc in a way that will produce a more undisturbed image of the jet at a higher resolution, which could prove invaluable in understanding the origin of the powerful outflows.

5.3 230 GHz simulations of M87*

In this section, I will present typical results of my simulated 230 GHz observations of the M87* model discussed in the previous section. For each simulation I present four relevant figures. The dirty map, the dirty beam, the residual map and the clean map. The dirty map, residual map and clean map show rms pixel values. Above the dirty beam is the theoretical rms noise of the image, based on integration time and site SEFDs. The clean map also shows S/N ratio of the image calculated as the maximum intensity pixel divided by standard deviation of the red off-source region.

The first simulation (Fig. 22) shows a 230 GHz observation of M87 excluding the Greenland Telescope. Residual map rms is 0.33% of clean map rms, suggesting a deep clean as adding the residual map to the image would not alter the clean map significantly. The theoretical rms noise of the dirty beam is 2.17×10^6 K. The dirty beam main lobe is not very well defined and shows some neighbouring clumps (sidelobes) of high sky-response. The

recovered image is not very good compared to the blurred model image, most likely caused by bad uv-coverage and not noise (S/N $\sim$ 389). The ring is not enclosed and the image is clumpy

The second simulation (Fig. 23) attempts to replicate the current EHT configuration, with the Greenland Telescope located at Thule. The residual rms is 0.18% of the clean map rms. The dirty beam is more defined due to the added GLT baselines, eliminating the neighbouring clumps from before. Due to the added thermal noise from GLT baselines the theoretical rms noise of the dirty beam is slightly increased to 2.43×10^6 K, by $\sim$ 12%. The added uv-coverage from the GLT baselines significantly improve the image quality. The image now resembles the blurred model image, an asymmetric ring with some structure extending from the lower part of the ring. The central depression is visible and is roughly a third of the width of the image scale (lower right in clean map), or $\sim 12\mu$as.

The third and final 230 GHz simulation (Fig. 24) attempts to estimate capabilities of EHT following the GLT relocation. In terms of image quality the clean map is largely similar, which is to be expected as the resulting uv-coverage is largely unchanged (more on this later). The residual map rms is 0.20% of the clean map rms, which is once again indicative of a deep clean. Due to the increase in GLT baseline sensitivities, the theoretical rms noise of the dirty beam is lowered to 2.31×10^6 K - a decrease of 5%. S/N ratio is lowered from before the relocation. The decrease in S/N is not isolated to this specific run, but is typical following the relocation. Possible explanations for this will be explored in coming sections.

In summary, each produced dirty map is cleaned until the residual map rms value falls below 1% of the clean map rms. The clean maps reveal the importance of GLT baselines for image recovery and the relocation lowers the theoretical rms array noise with about 5%. Image quality does not seem to be effected by the relocation of GLT.

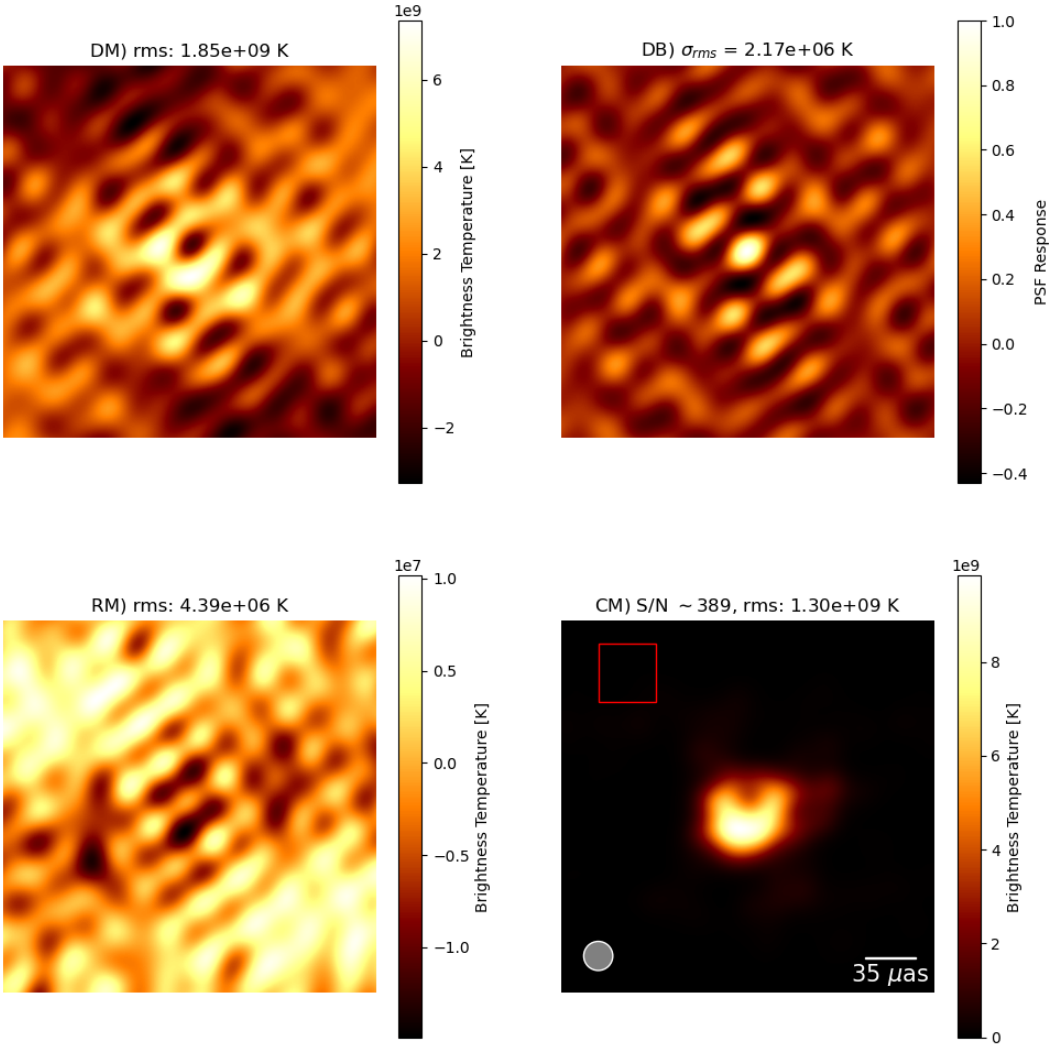

Figure 22: Simulated 230GHz VLBI observation of M87* with the 2020 EHT configuration excluding the Greenland Telescope. Campaign starts at 01^{h} UTC and ends at 09^{h} UTC, with 300 second on-source integration occurring every 20 minutes. Bandwidth is 4GHz. The four figures represent the dirty map (DM; upper left), dirty beam (DB; upper right), residual map (RM; lower left) and clean map (CM; lower right).

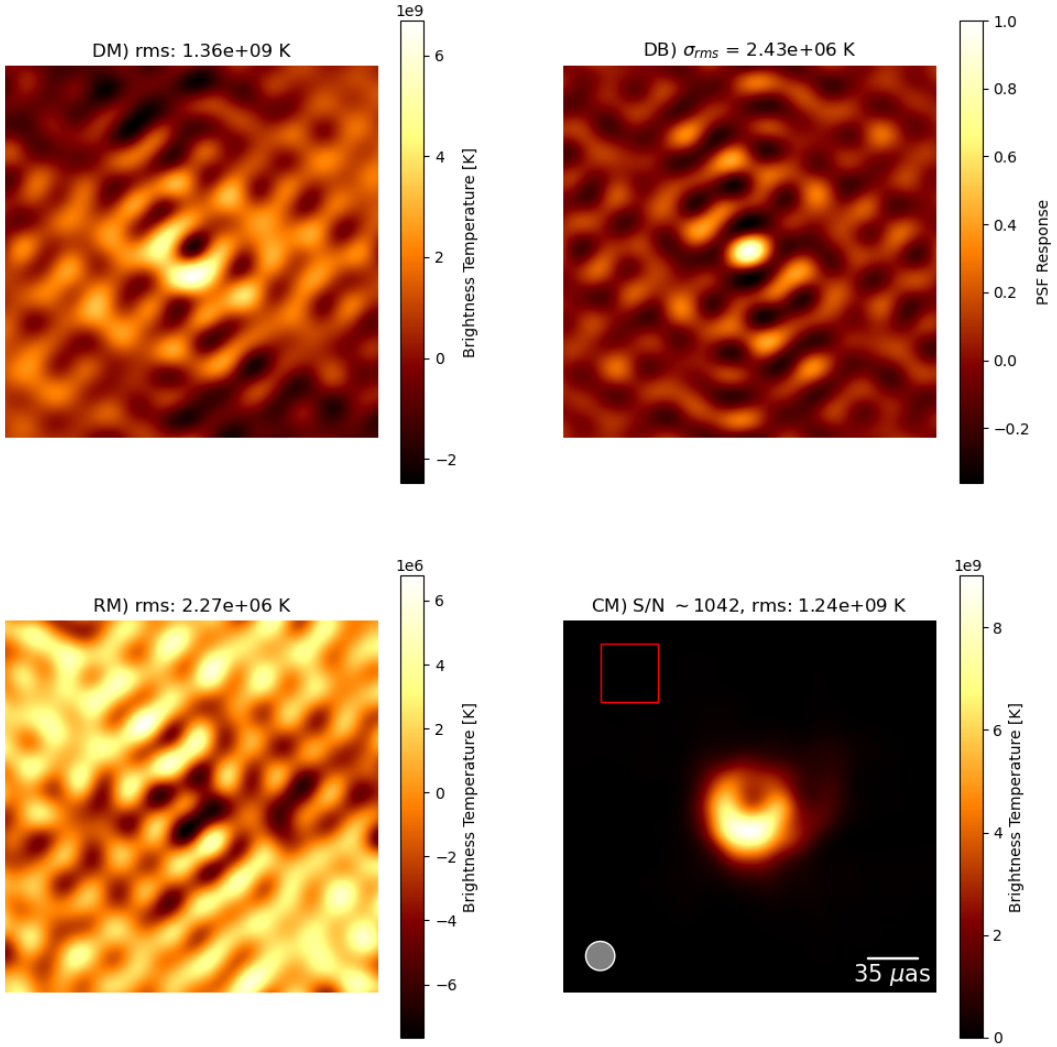

Figure 23: Simulated 230GHz VLBI observation of M87* with the 2020 EHT configuration including the Greenland Telescope, located at Thule. Campaign starts at 01^{h} UTC and ends at 09^{h} UTC, with 300 second on-source integration occurring every 20 minutes. Bandwidth is 4GHz. The four figures represent the dirty map (DM; upper left), dirty beam (DB; upper right), residual map (RM; lower left) and clean map (CM; lower right).

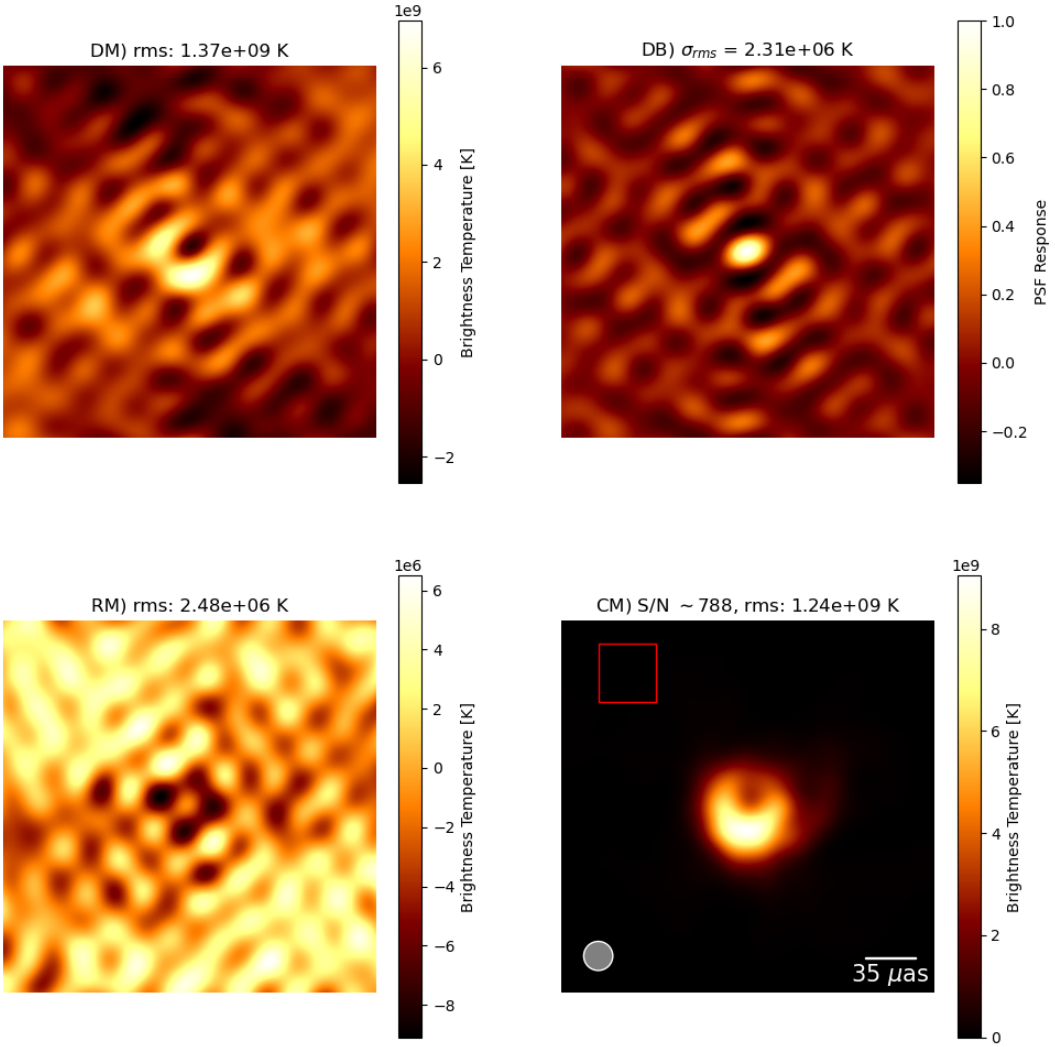

Figure 24: Simulated 230GHz VLBI observation of M87* with the 2020 EHT configuration including the Greenland Telescope, located at the Summit Camp. Campaign starts at $01^{\rm h}$ UTC and ends at $09^{\rm h}$ UTC, with 300 second on-source integration occurring every 20 minutes. Bandwidth is 4GHz. The four figures represent the dirty map (DM; upper left), dirty beam (DB; upper right), residual map (RM; lower left) and clean map (CM; lower right).

5.4 230 GHz EHT sensitivity

From the National Radio Astronomy Observatory website[25] the theoretically expected thermal noise for an image produced using natural weighing of the visibility data is given by

$$\Delta I = \frac{SEFD}{\eta_c \sqrt{n_p N(N-1) t_{int} \Delta\nu}} \tag{47}$$

where η_c is the correlator efficiency, n_p is the number of polarizations, N is the number of antennae (or stations), t_{int} is the total integration time and $\Delta\nu$ is the bandwidth. For the system equivalent flux density I use the geometric mean of included non-identical antennae, i.e.

$$SEFD_{1,2,...,n} = \sqrt{SEFD_1 \times SEFD_2 \times ... \times SEFD_n}. \tag{48}$$

I wanted to compare this equation with the simulation output, so I created an array configuration file containing only the ALMA-GLT(Thule) baseline and ran simulations of varying on-source integration times, weighing the data using the natural weighing scheme. I plotted the simulation output thermal rms-noise in the image and over-plotted expected noise values, using the equation above, for $\eta_c = 0.8 \pm 0.1$. Results are shown in Fig. 25. As is

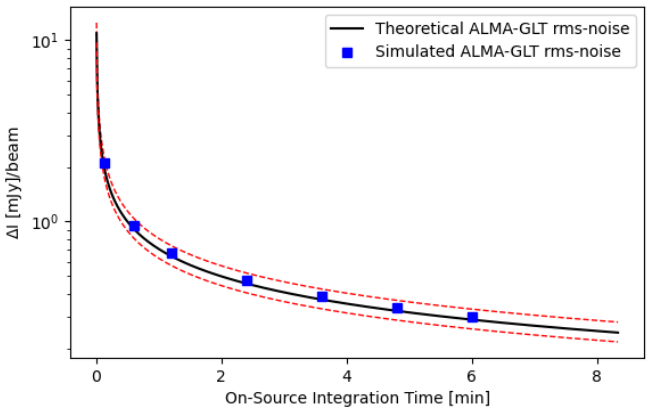

Figure 25: Theoretical vs. simulated image rms-noise values, assuming natural weighing of the visibility data. Solid line indicates $\eta = 0.8$ with surrounding dashed lines indicating ± 0.1.

evident, the simulation code returns the theoretically expected rms noise values for multiple instances of total on-source integration times. I use this result to double check the output of the simulation which is in accordance with theoretically expected values. The theoretical equation *could* be used to estimate the sensitivity of the Event Horizon Telescope as a

[25] `https://science.nrao.edu/facilities/vla/docs/manuals/oss/performance/sensitivity`

whole, but only under the assumption that each station will share the same total on-source integration time, which is not the case, thus I must use the output of the simulation. Having confirmed that the code returns theoretically expected values, I ran multiple EHT 230 GHz observations with increasing total on-source integration time for the three different configurations and recorded the rms-image noise using natural data weighing. Fig. 26 shows the result. It is hard to tell the increase in array sensitivity following the relocation when

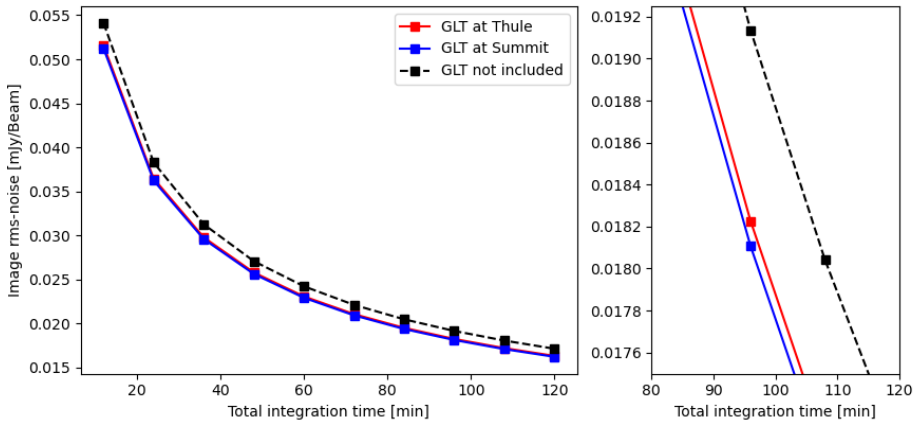

Figure 26: rms-noise of synthesized EHT beam (230GHz) using natural weighing as a function of total on-source time integration. Values obtained from simulated synthetic data using SEFD values from Table 2 and updated GLT SEFD from Table 6.

observing at 230 GHz, but one must recall that the contribution of collecting area that GLT supplies to EHT as a whole is very small, as illustrated in Fig. 27. GLT is clearly one of

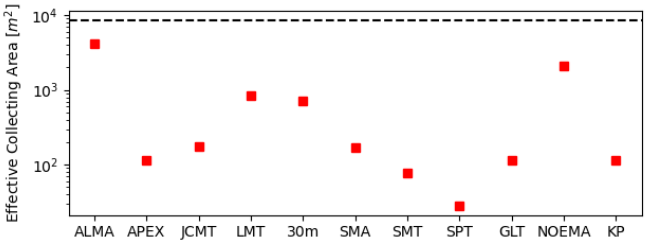

Figure 27: Effective collecting area of the 11 stations in the EHT network. The black dashed line marks the total effective collective area of 8638m^2.

the smaller contributors and constitutes only about 1.3% of the total collecting area. Main contributors are the phased ALMA array ($\sim$ 50%), NOEMA ($\sim$ 25%), LMT ($\sim$ 10%) and

the 30m telescope ($\sim 10\%$) with the remaining stations contributing less than 3% each. The more a particular site contributes to the total collecting area, the more impact changes to that specific site will have on EHT as a whole. As such, the Greenland Telescope's small contribution is a probable cause to the low decrease in measured image noise following the relocation. While collecting area is an important part of the sensitivity (SEFD $\propto D^{-1}$), station positions play an enormously important role as well, as they determine which spatial frequencies are sampled. While small dish antennae, such as GLT, might not collect as much light as ALMA, NOEMA, JCMT and LMT, they still serve an important role in sampling, as they open up more possible signal correlation windows during an observation campaign, which yields more uv-coverage.

An important note is, that due to the natural weighing of the visibility data used in this calculation, as opposed to the uniform weighing used in the imaging, the sensitivities of the three configurations have been shifted. The configuration excluding GLT is now the least sensitive while the configuration with GLT at Summit is the most sensitive.

5.5 Estimating 345 GHz site sensitivity

In this section I will attempt to estimate the 345 GHz site sensitives, as this information is not readily available. I will need this information in order to perform simulated 345 GHz observations with appropriate station thermal noise errors. In order to estimate the 345 GHz SEFD of each station I have worked from one assumption, namely that the aperture efficiency of each station remains largely the same for 230 GHz and 345 GHz receivers / bands, which allows me to assume, using eq. (43), that

$$\mathrm{SEFD} \propto \mathrm{T_{sys}} \tag{49}$$

which can be used to infer a simple scaling relation

$$\mathrm{SEFD}_2 = \frac{\mathrm{T_{sys,2}}}{\mathrm{T_{sys,1}}} \times \mathrm{SEFD}_1. \tag{50}$$

Assuming that 1 = 230 GHz, 2 = 345 GHz and utilizing known station specific 230 GHz values, all I need to estimate 345 GHz sensitivities is the station specific system temperature when operating their respective 345 GHz receivers. This information can be located using websites, tools and technical documents associated with each of the stations. Not all stations are currently equipped to perform 345 GHz observations and these will be excluded from my 345 GHz simulations. Not all sites, documents, or tools specify, or allow for specification of season, i.e. summer or winter, which can have a large impact on sensitivity. In cases where I have a choice, I will adopt reported typical values for the Winter seasons, under good conditions. In cases where only 350 GHz values are available I will assume $\mathrm{T_{sys,350GHz}} \approx \mathrm{T_{sys,345GHz}}$. When using sensitivity estimators, I use astronomy software Stellarium[26] to

[26] `http://stellarium.org/`

estimate typical source elevation in the sky, assuming target source is M87*, which can be done by choosing an observation location and target, and calculating source elevation vs. time and determining an average.

The *ALMA* 345 GHz system temperature can be located in the cycle 7 ALMA Technical Handbook (Remijan et al. [2019]). The > 200 page document is from 2019 and is an in-depth technical overview of the 7th cycle of the aperture synthesis array. In chapter 4.2.5, regarding the Band 7 (275-373 GHz) receiver, figure 4.23 shows typical system temperature for zenith observations at a variety of frequencies. For a typical PWV value at the Chile site ($\sim$ 1mm), I read $T_{sys} \sim 170$K. From table 9.3 in the document they list the aperture efficiencies for the different bands. For band 6 these are 0.68 and 0.69 for 12m and 7m antennae respectively. For band 7 these lower only to 0.63 and 66, thus I deem that my aforementioned approximation holds true for ALMA.

The *APEX* 345 GHz system temperature can be found at the Atacama Pathfinder Experiment website, under the APEX observatory system tab[27]. On the site they report that the APEX-2A heterodyne reciever (279-381 GHz) has typical double-side-band (DSB) system temperatures upwards of 150 K but up to 250 K when tuning to 370 GHz. Using this information, I estimate an APEX 345 GHz $T_{sys} \sim 225$ K. I could not locate any 345 GHz aperture efficiency.

Buckle et al. [2009] describe the HARP/ACSIS (325-375 GHz) system in place at the *JCMT* observatory. They report single side band system temperatures of about $T_{sys} \sim 300$ K under good conditions. On the JCMT website, under the HARP tab[28], they report an aperture efficiency of 0.52, which is the same as for the 230 GHz receiver.

For *SMA* the necessary information is available on a spec-sheet on their website[29]. They report that the 345 GHz receiver exhibits system temperatures between 150-350 K. For my purposes I choose to approximate $T_{sys} \sim 300$ K. They also report 345 GHz aperture efficiencies ranging from 0.60-0.75, which is close to the reported 230 GHz efficiency.

The *LMT* has only developed capability for VLBI observations at 1.3 mm and 3 mm wavelengths[30]. Due to this constraint, the Large Millimeter Telescope will be excluded from the following 345 GHz simulations.

The *30-meter telescope* atop Pico Veleta has a sensitivity estimator on its website[31]. When observing 345 GHz frequency radiation from a source at a typical declination of ~ 30 degrees in good conditions, I estimate a $T_{sys} \sim 712$ K during the winter season, using the 30m-EMIR band 3 (E3) receiver. I could not locate any 345 GHz aperture effeciency.

For *NOEMA*, I located a short 7 page technical document describing sensitivity estima-

[27] http://www.apex-telescope.org/mirror/observations/observing/febe.html
[28] https://www.eaobservatory.org/jcmt/instrumentation/heterodyne/harp/
[29] http://sma1.sma.hawaii.edu/specs.html
[30] http://lmtgtm.org/telescope/instrumentation/general-information/
[31] https://www.iram.es/nte/

tion for the synthesis array (Pety et al. [2015]). In Table 1, they report system temperatures for NOEMA in proposal mode. Specifically they state that the band 4 receiver (277-370 GHz) exhibits winter system temperatures of about $T_{sys} \sim 370$ K. I could not locate the 345 GHz aperture efficiency for the NOEMA array.

For *SMT* and the *Kitt Peak* observatories I found technical status reports from 2019 by the Arizona Radio Observatories[32]. In this short document it is reported that the Kitt Peak observatory does not have 345 GHz receivers in place yet and will therefore be excluded from the following simulations. The Sub-Millimeter Telescope does have a 0.8 mm receiver (325-370 GHz) which is reported to have typical system temperature around 600-900 K, for which I'll assume $T_{sys} \sim 750$ K, but I could not locate the 345 GHz aperture efficiency.

As mentioned in the array section, the South Pole Telescope cannot observe M87* and as such, it will also be excluded from my 345 GHz observations.

Finally, Information regarding *GLT* was obtained through correspondence with Satoki Matsushita and is shown in Table 6. For the Greenland Telescope I do not assume equal aperture efficiencies between 230 GHz and 350 GHz observations. The 350 GHz SEFD is calculated using the aperture efficiency supplied by Matsushita.

All discussed system temperatures, as well as estimated system equivalent flux density for the 345 GHz ready Event Horizon Telescope array, are summarized in Table 7.

5.6 345 GHz simulations of M87*

Based on my estimations of the 345 GHz site capabilities, I simulate 345 GHz observations of the M87* model. Just as for the 230 GHz, I will present three typical runs using three configurations; no GLT, GLT at Thule and GLT at the Summit Camp. As determined in the previous section, the Kitt Peak (KP) telescope and Large Millimeter Telescope (LMT) are not equipped with 345 GHz receivers and are not part of these simulations.

The first 345 GHz simulation (Fig. 28) does not include the Greenland Telescope. The residual map rms value is 2.27% of the clean map rms. This indicates a CLEAN that has not been as thorough as the 230 GHz counterpart, although still acceptable. The dirty beam rms noise has doubled compared to the 230 GHz counterpart, at 4.31×10^6 K. This is expected due to the increased thermal noise present at each site, at 345 GHz. Image quality is very poor, which is also expected as not only is GLT excluded from this observation, but also KP and LMT which greatly impacts the uv-coverage. This results in an image that does not resemble the blurred model. The main lobe of the dirty beam is not well defined and there is a lot of high sidelobe sky response.

The second 345 GHz simulation (Fig. 29) includes GLT at Thule. Residual rms is 1.29% of the clean map rms, slighly better than before, but still not as thorough as the 230 GHz counterpart. Image quality is greatly enhanced due to the addition of GLT baselines, but

[32] `https://www.as.arizona.edu/sites/default/files/AROstatus30Jul2019-compressed.pdf`

Site	230GHz, T_{sys} [K]	345GHz, T_{sys} [K]	345GHz, SEFD [Jy]
ALMA	76	170	166
APEX	118	225	8962
JCMT	345	300	9130*
SMA	285	300	6526
LMT	371		
30m	226	712	5986
SMT	291	750	44072
SPT	118		
GLT(t)	120	350	14009
GLT(s)	105	200	8005
NOEMA	270	370	959
KP	310		

Table 7: Table showing expected 230GHz and 345GHz system temperatures for all concurrent EHT stations, as well as estimated 345GHz SEFD. Red entries denote stations not included in the simulation, either due to lacking capability (LMT/KP) or position (SPT).
*The increase in sensitivity for *JCMT* is a result of the new HARP receiver, replacing the RxA for 345GHz observations.

just as for the 230 GHz simulation, dirty beam rms-noise has increased slightly to 4.48×10^6 K, which is an increase of 4%. The main lobe is more defined, but still exhibits some neighbouring clumps above and below the central region. The recovered images resembles the blurred model well, and the central depression is easily visible, surrounded by the asymmetric ring, as well as the small structure extending from lower region.

The final simulation (Fig. 30) relocates GLT to the Summit Camp. Residual rms is 1.32% of clean map rms. Image quality remains largely unchanged. GLT sensitivity increase lowers dirty map rms-noise to 4.20×10^6 K, a decrease of 6.25%. The leap in rms-noise following the relocation is expectantly larger for 345 GHz, as the receiver is estimated to be impacted more by the relocation than the 230 GHz receiver. The neighbouring sidelobe clumps above and below the central region in the dirty beam seem slightly less distinct following the relocation. The S/N ratio is once again lowered slightly following the relocation, but does not seem to impact the image quality.

In summary, the GLT baselines are crucial in order to recover an image that resembles the blurred model. Theoretical rms-noise is roughly doubled when observing in 345 GHz, but slightly lowered following the relocation of GLT to the Summit Camp. M87* can be observed through 345 GHz radiation with GLT located at Thule, under the assumption that

atmospheric conditions are stable above the site, but current estimates on GLT thermal noise do not seem to be a limiting factor.

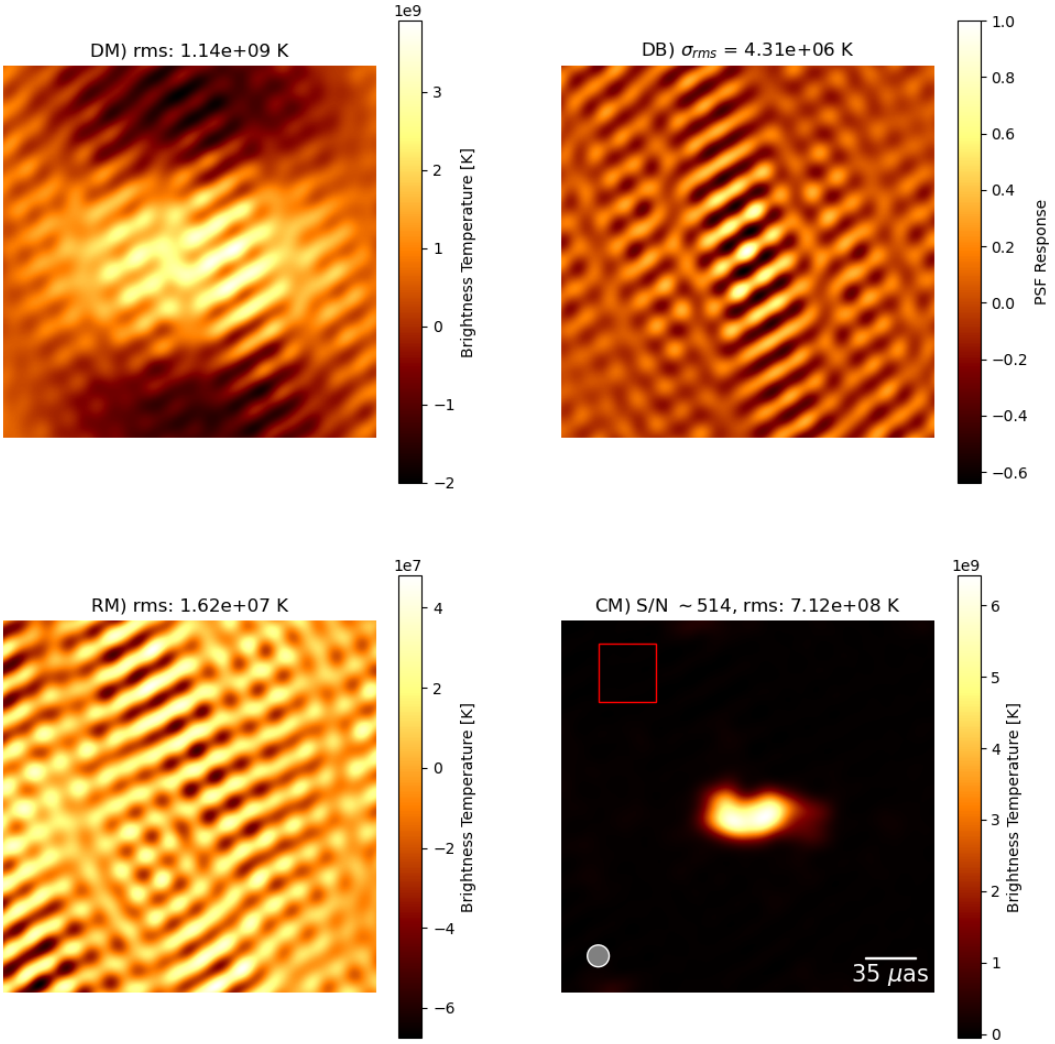

Figure 28: Simulated 345GHz VLBI observation of M87* with the 2020, 345GHz ready EHT configuration excluding the Greenland Telescope. Campaign starts at 01^{h} UTC and ends at 09^{h} UTC, with 300 second on-source integration occurring every 20 minutes. Bandwidth is 4GHz. The four figures represent the dirty map (DM; upper left), dirty beam (DB; upper right), residual map (RM; lower left) and clean map (CM; lower right).

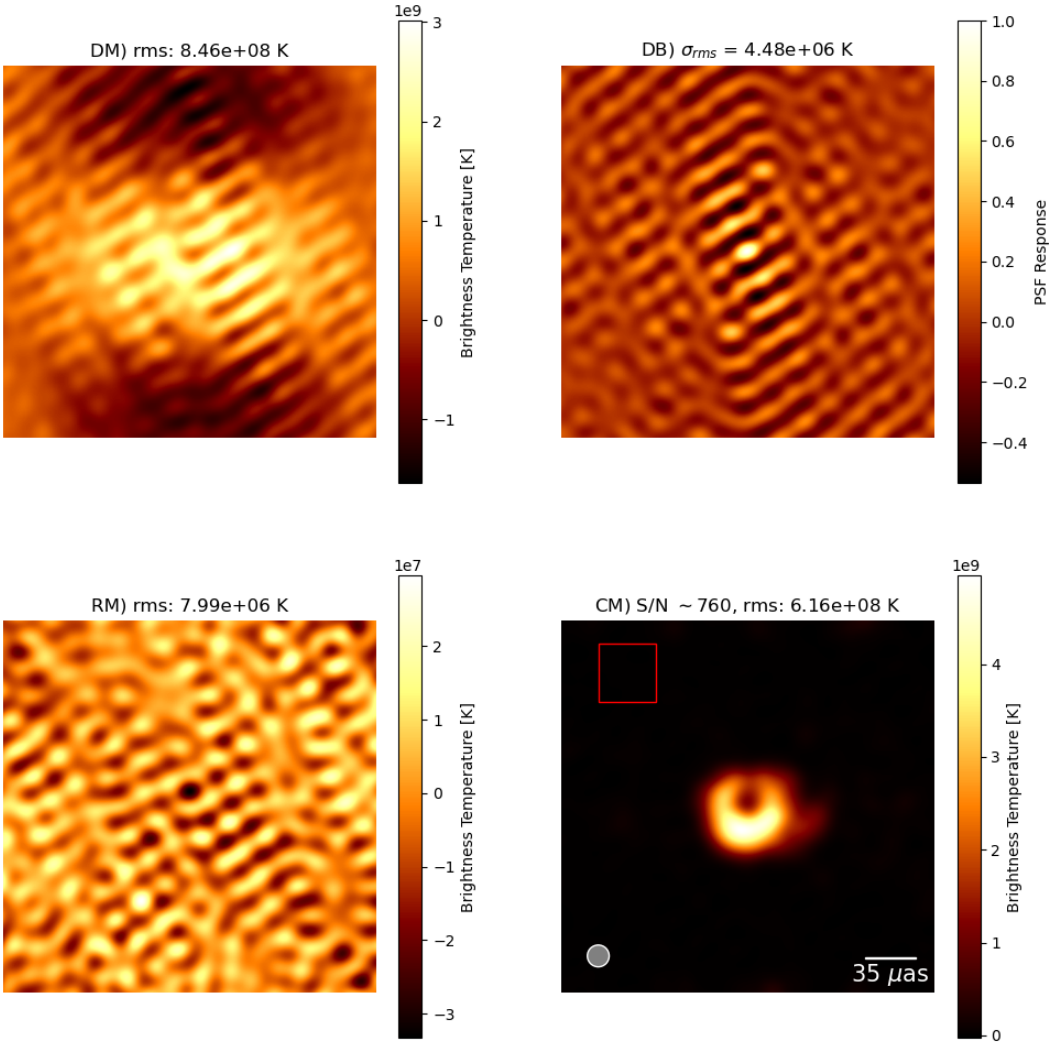

Figure 29: Simulated 345GHz VLBI observation of M87* with the 2020, 345GHz ready EHT configuration including the Greenland Telescope, located at Thule. Campaign starts at 01^{h} UTC and ends at 09^{h} UTC, with 300 second on-source integration occurring every 20 minutes. Bandwidth is 4GHz. The four figures represent the dirty map (DM; upper left), dirty beam (DB; upper right), residual map (RM; lower left) and clean map (CM; lower right).

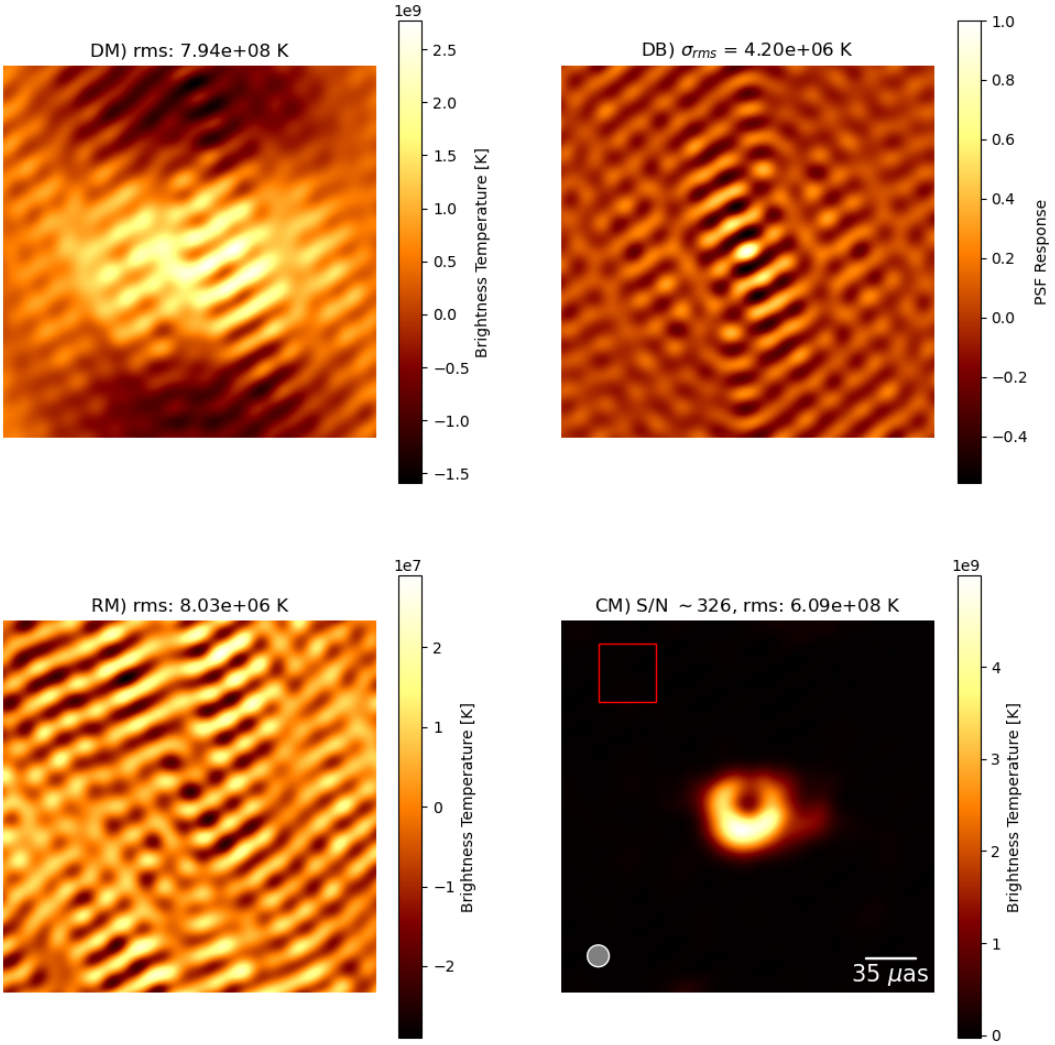

Figure 30: Simulated 345GHz VLBI observation of M87* with the 2020, 345GHz ready EHT configuration including the Greenland Telescope, located at the Summit Camp. Campaign starts at 01^{h} UTC and ends at 09^{h} UTC, with 300 second on-source integration occurring every 20 minutes. Bandwidth is 4GHz. The four figures represent the dirty map (DM; upper left), dirty beam (DB; upper right), residual map (RM; lower left) and clean map (CM; lower right).

5.7 345 GHz EHT sensitivity

Just as for the 230 GHz observations, I inspect the 345 GHz rms-noise of the synthesized EHT beam over differing integration times, for the three configurations. Fig. 31 shows the results.

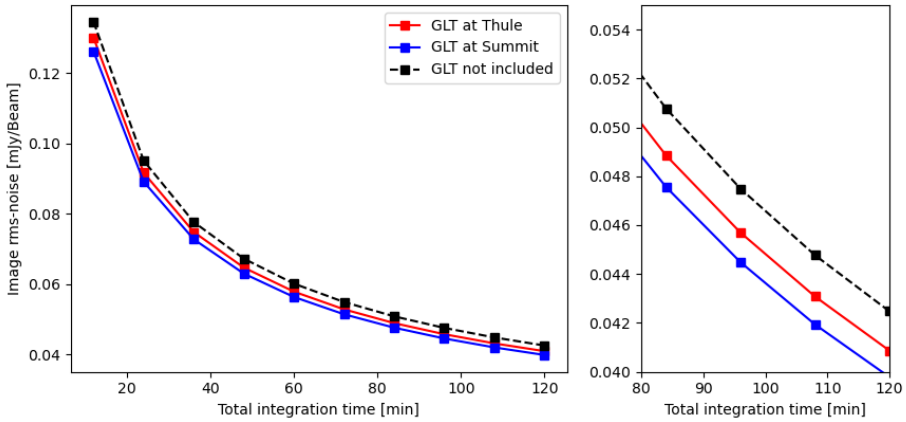

Figure 31: rms-noise of synthesized EHT beam (345GHz) using natural weighing as a function of total on-source time integration. Values obtained from simulated synthetic data using SEFD values from Table 7 and updated GLT SEFD from Table 6.

When observing 345 GHz radiation the effect from relocating GLT is more noticeable, yet still small, which is once again owed to the small dish size of the Greenland Telescope. Comparing Fig. 26 to Fig. 31 one will see that for 230 GHz, rms noise-levels of 4 μJy/beam are achieved after $\sim$ 20 min of on-source integration time, while for 345 GHz observations this is only achieved after the entire observation has been concluded at $\sim$ 120min. In other words, when observing 345 GHz radiation, the integration time must be 6 times longer to achieve comparable noise levels to observations of 230 GHz radiation. While the leap in sensitivity is larger following the relocation of GLT, at 345 GHz, the overall sensitivity is still lower when compared to 230 GHz observations, which is to be expected.

5.8 Visibility amplitudes and uv-coverage

In this section, I will inspect changes in uv-coverage and sampled visibility amplitudes across all my simulations. Based on the recovered images from my simulations, the relocation of GLT should not result in any significant alteration to the sampled Fourier visibilities, but simply including GLT should significantly enhance uv-coverage which, alongside the visibility amplitude vs. uv distance for the 230 GHz simulations, are shown in Fig. 32.

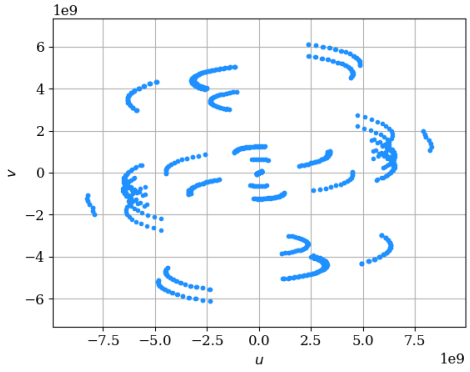

(a) uv-coverage, no GLT

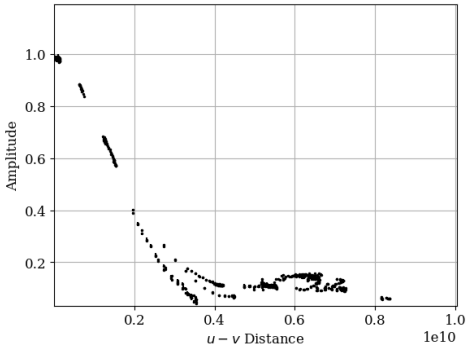

(b) Vis. amplitude, no GLT

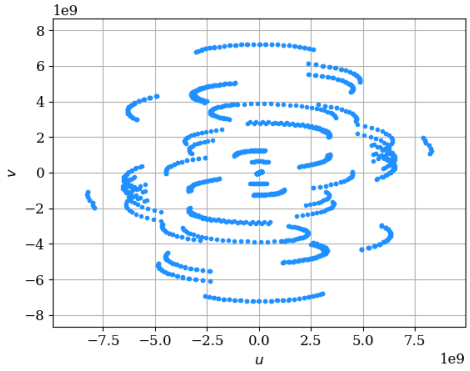

(c) uv-coverage, GLT at Thule

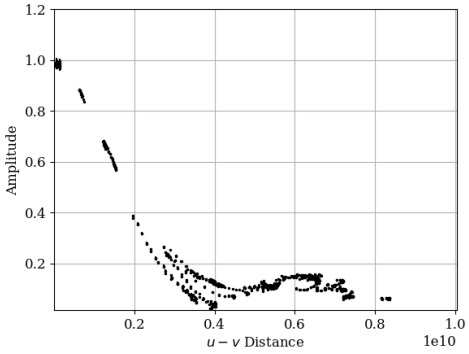

(d) Vis. amplitude, GLT at Thule

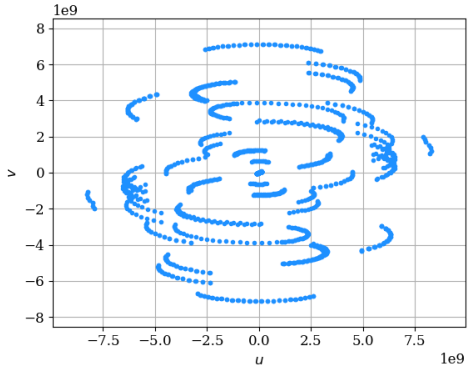

(e) uv-coverage, GLT at Summit

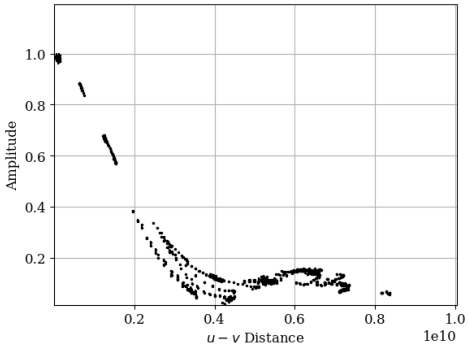

(f) Vis. amplitude, GLT at Summit

Figure 32: uv-coverage and visibility amplitude vs. uv-distance for each **230GHz** simulation configuration. Campaign spans 8 Hours (01^{h} to 09^{h} UTC) with 300s (5min) scans occurring each 1200s (20min).

As is evident the uv-coverage sees great improvement by including the Greenland Telescope in the observation. The upper- (and lower-)most uv-tracks are spanned by GLT-ALMA and GLT-APEX baselines and function as high resolution samplers during the observation. Visibillites sampled at uv-distances $> 0.8 \times 10^{10}\lambda$ (10400 km) are produced by stations Noema, JCMT, SMA and the 30m telescope. At this separation very little correlated flux

$$S_{\rm cor} \sim A_{\rm vis} F_{\nu,\rm tot} \tag{51}$$

is measured (< 0.1 Jy). The addition of GLT populates the region $\sim 0.2 - 0.7 \times 10^{10}\lambda$ (2600 km - 9100 km) with many new visibility samples, which are responsible for the upgraded image quality. Corresponding uv-coverage and visibility amplitude plots for my 345 GHz simulations are shown in Fig. 33.

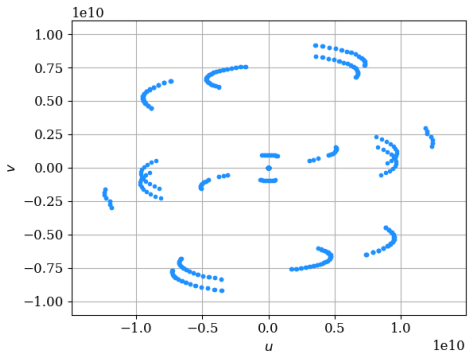

(a) uv-coverage, no GLT

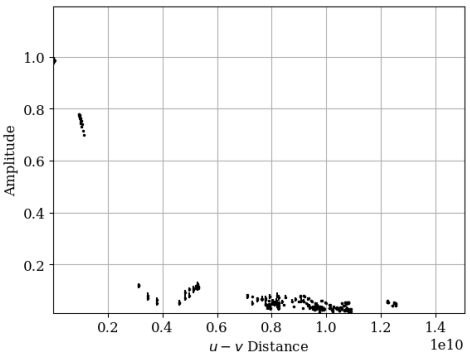

(b) Vis. amplitude, no GLT

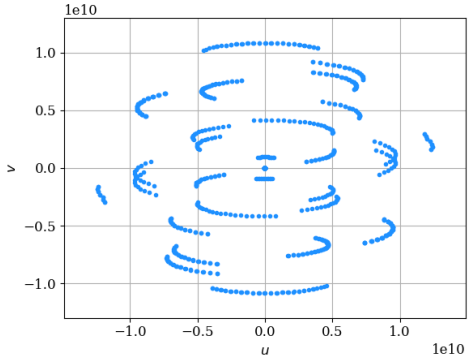

(c) uv-coverage, GLT at Thule

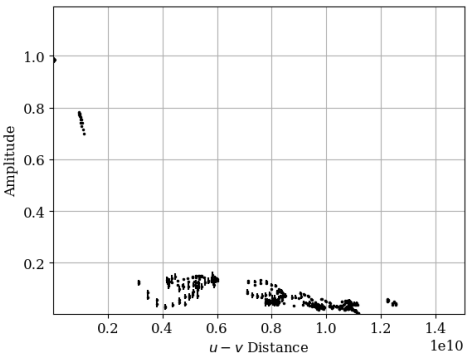

(d) Vis. amplitude, GLT at Thule

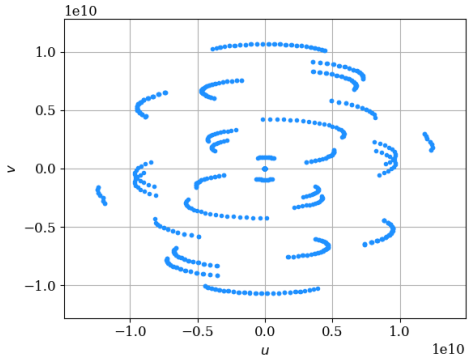

(e) uv-coverage, GLT at Summit

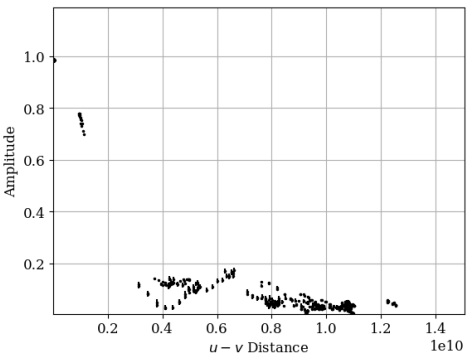

(f) Vis. amplitude, GLT at Summit

Figure 33: uv-coverage and visibility amplitude vs. uv-distance for each **345GHz** simulation configuration. Campaign spans 8 Hours (01^{h} to 09^{h} UTC) with 300s (5min) scans occurring each 1200s (20min).

The absence of GLT, LMT and KP yields a sparse uv-coverage as seen in Fig. 33a. Upon re-including GLT, the lackluster uv-coverage is slightly remedied, although not as complete

as for 230 GHz. GLT baselines populate uv-distances between $0.3 - 1.1 \times 10^{10}\lambda$ (2610 km - 9570 km) which agrees with the region populated during the 230 GHz observations. For both observing frequencies, we lack uv-coverage to sample all parts of the initial amplitude drop, responsible for measuring large scale emission.

5.9 Simulation statistics

In this section I will present signal-to-noise (S/N) statistics of my simulations. Thermal noise introduces random Gaussian errors for each site, determined by site SEFD, during each simulated observation. To get a better idea of typically achievable S/N ratios before and after the relocation of GLT, I ran 200 simulations varying postion and observing frequency every 50th observation. Fig. 34 show the results. where S/N is defined as

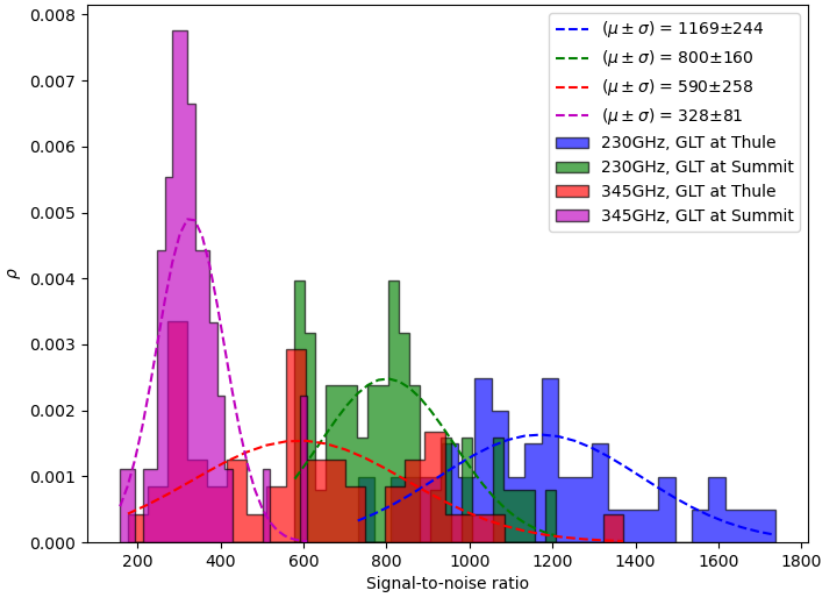

Figure 34: Histogram of recorded S/N values across 200 simulated observations of M87* model. Dashed lines are normal distribution fits of the data.

$$\text{S/N} = \frac{\text{Maximum clean map value}}{\text{Standard deviation of off-source region}} \tag{52}$$

where the *off-source region* is marked in red on my CLEAN maps. As already seen in the previous sections, I typically observe a lowering in S/N ratio following the relocation of GLT

(for both observing frequencies), which does not seem to match the expectation that the array noise should be lowered. Mean values show a drop in 31.6%, for 230 GHz, and 44.4% for 345 GHz. There may be a number of reasons that could cause this: First, the standard deviation of the off-source background region is wholly dependant on how well, and *where*, the dirty map is cleaned. Secondly, the choice of imaging weights significantly alter noise levels in the image.

Inspecting four separate log-scale 230 GHz clean maps for both GLT positions, I can get a better understanding of the structure of the background noise after the image has been cleaned - see Fig. 35. Some patches of my clean maps will exhibit negative values in orders of -10^{-4} Jy/beam (maximum clean map values are in the order of 10^{-1} Jy/beam). This occurs as the cleaning procedure is set to halt at the first negative component created while cleaning. As these maps are logarithmic, negative values will results in "NaN" values (white patches in the map), but due to their low magnitude in comparison to the maximum map value, these can be approximated as ~ 0 Jy/beam.

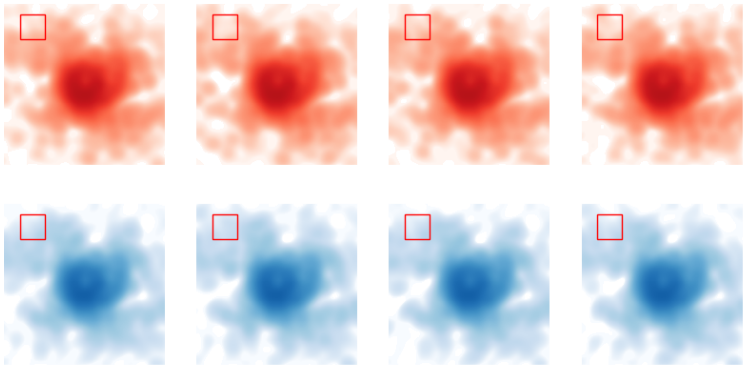

Figure 35: Logarithmic scale CLEAN maps, from simulated **230GHz** observations. Red maps are generated with GLT at Thule. Blue maps are generated with GLT at Summit. The data has been imaged using uniform weighing of visibility data.

As is evident, the background noise level for 230 GHz simulations is structurally consistent over multiple simulations. Corresponding logarithmic clean maps for 345 GHz simulations are shown in Fig. 36.

The presence of negative patches resulting in NaN values are far more prominent in these maps, but are still somewhat consistent across multiple runs. This leads me to believe that my choice of *where* to locate my off-source region is not a significant contributor to lowering

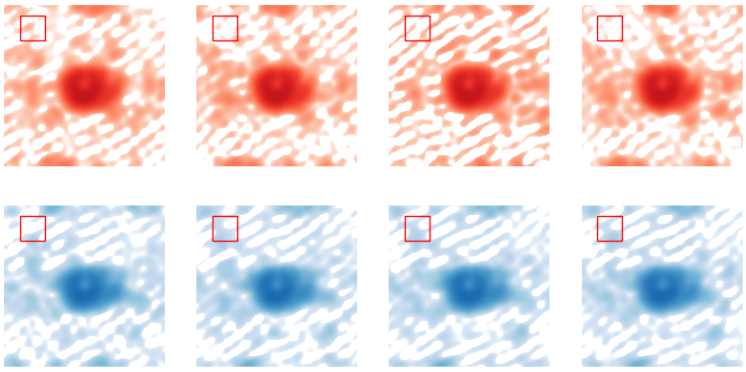

Figure 36: Logarithmic scale CLEAN maps, from simulated **345Ghz** observations. Red maps are generated with GLT at Thule. Blue maps are generated with GLT at Summit. The data has been imaged using uniform weighing of visibility data.

the S/N ratio, but the values within the region might be. In order to quantify and test these values, I have done 10 simulations for each of the four configurations above. For each simulation, I record the standard deviation from my marked region, as well as the maximum and minimum image values. Fig. 37 show the results.

The maximum clean map values are mostly constant and unaltered by the GLT relocation, but is lowered by $\sim$ 30% when observing 345 GHz radiation, which limits the maximally achievable S/N ratio. The standard deviation of the off-source region varies for each simulation as the CLEAN algorithm works from slightly different initial conditions set by random thermal errors. For both observing frequencies, the standard deviation of the background off-source region is larger following the relocation. This helps to explain the difference in my observed S/N ratios, as well as the fitted standard deviation on mean S/N values. As my S/N value is $\propto \frac{1}{\sigma_{\text{region}}}$, higher values of mean region standard deviation will result in a more narrow distribution width. Minimum image values are seen to be slightly lowered when cleaning the 345 GHz dirty maps, but magnitudes are still comparatively low to the maximum image value. The presence of negative image values in the same order-of-magnitude as the calculated region standard deviation is not ideal. This effectively increases the region standard deviation[33] - which lowers the S/N ratio. This effect is worst for 345GHz simulations, where minimum image values fall to ~ -0.0006 Jy/beam. One solution to this, would be an improved DIFMAP imaging script which works at a lower gain

[33]If the negative values were lower orders-of-magnitude this effect could be ignored.

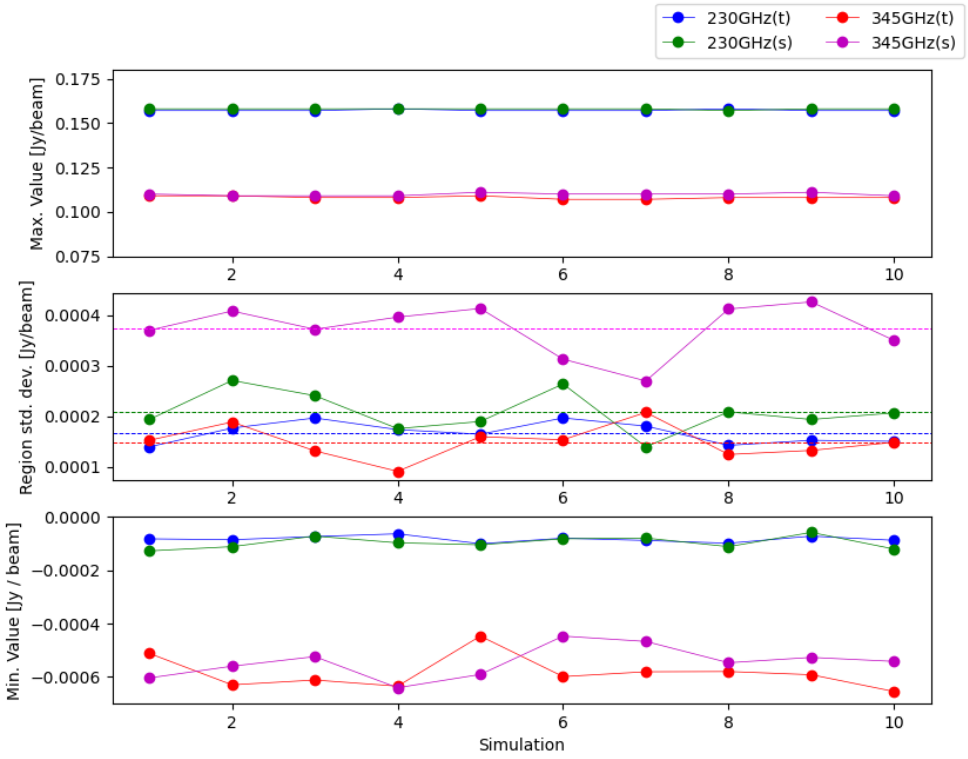

Figure 37: Recorded Maximum and Minimum Jy/beam image values and standard deviation of the marked red region. "t" and "s" refers to whether GLT is located at Thule (t) or Summit (s). Dashed lines indicate standard deviations means. From top to bottom these are: 0.000373, 0.000208, 0.000168 and 0.000149 Jy/beam.

value and halts before negative components (more on this will follow in the discussion). If one instead chooses to define S/N ratio as

$$\text{S/N} = \frac{\text{Maximum clean map value}}{\text{Theoretical rms-noise}} \tag{53}$$

using natural weighing of the visibility data, the results would be flipped and simulations with GLT at Summit would consistently show highest S/N values (see sensitivity sections).

5.10 Single Baseline Inspection

This section will focus on the impact of the relocation on single baselines instead of EHT as a whole.

During 230 GHz campaigns the Greenland Telescope creates nine baselines. These are ALMA-GLT, APEX-GLT, NOEMA-GLT, LMT-GLT, 30m-GLT, SMA-GLT, JCMT-GLT, KP-GLT and SMT-GLT. For 345 GHz campaigns KP and LMT baselines are excluded which leaves a total of seven baselines. I use eq. (44) to estimate the achievable S/N ratio during a single scan for each of these baselines. In order to estimate the correlated flux, I make use of the DIFMAP tool `vplot` which allows me to inspect measured visibility amplitudes during the observation campaign. While the measured amplitudes vary as the projected baseline distance is changed throughout the campaign, it is possible to estimate a mean amplitude for use in estimating correlated flux, assuming a total source flux of $\sim$ 1 Jy. Achievable S/N ratios when observing 230 GHz radiation from the M87* model for both GLT positions are shown in Fig. 38. The ALMA-GLT baseline exhibits the highest S/N

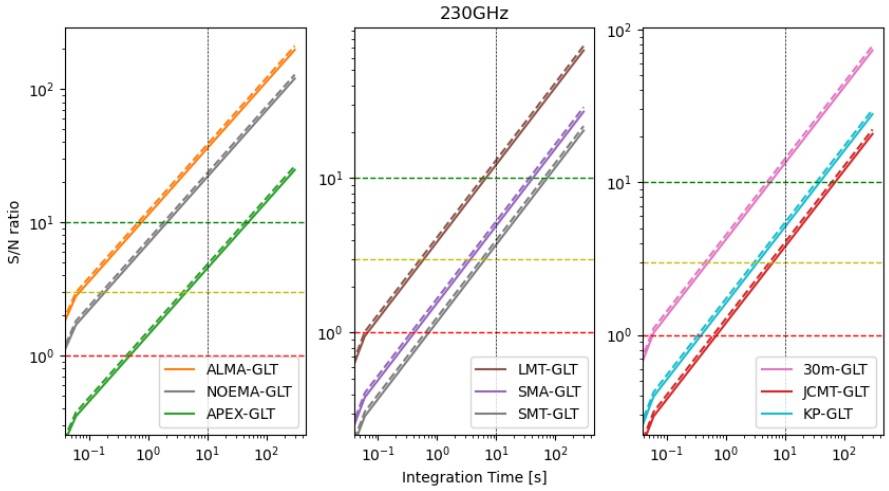

Figure 38: Expected S/N ratio vs integration time for GLT baselines during 230GHz observations. Solid lines indicate performance with GLT at Thule, dashed lines indicate performance for GLT at Summit. Green, yellow and red dashed horizontal lines indicate S/N values of 10, 3 and 1 respectively. Vertical black dashed lines indicates integration time of 10s.

gain pr. unit time, but is not the only baseline which achieves optimal (> 10) S/N ratio before 10 seconds, at which atmospheric fluctuations become problematic. The NOEMA-GLT, 30m-GLT and LMT-GLT baselines are also capable of this. Remaining baselines just about manage to surpass the S/N cutoff limit (< 3) at 10 seconds, revealing the necessity for longer integration times, allowed for by the two-stage detection approach described in earlier sections. For 230 GHz campaigns, there is a fleeting difference between achievable S/N ratios on the GLT baselines, for the different GLT positions, but all S/N gain rates are

slightly improved.

Expected S/N ratio vs. integration time for 345 GHz campaigns are shown in Fig. 39. For 345 GHz observations, achieving optimal S/N ratios within short timescales is more

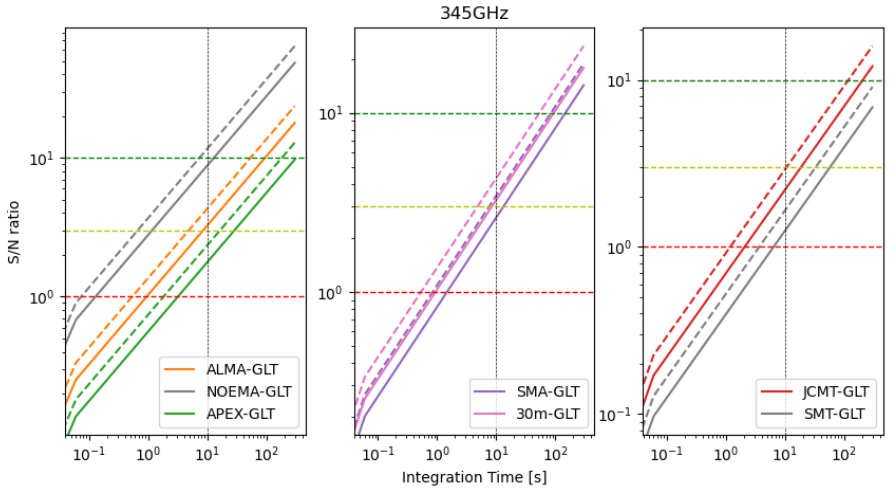

Figure 39: Expected S/N ratio vs integration time for GLT baselines during 345GHz observations. Solid lines indicate performance with GLT at Thule, dashed lines indicate performance for GLT at Summit. Green, yellow and red dashed horizontal lines indicate S/N values of 10, 3 and 1 respectively. Vertical black dashed lines indicates integration time of 10s.

challenging due to the increase in resolution, which lowers the amount of recovered signal for all baselines. In other words, the reduced beam size results in less source flux being integrated. The ALMA-GLT baseline is significantly impacted by this, lowering the S/N gain rate below that of the NOEMA-GLT baseline. It should be noted, that the expected correlated flux on a single baseline is *very* dependant on the model structure. As such results may vary greatly, depending on input model image. Long integration times are essential for acceptable detections at 345 GHz, but this is helped by the updated GLT position, which shows a more significant change in S/N gain rate upgrade for this observing frequency.

6 Discussion

In this section, I will discuss certain aspects of my method, possible issues and different tools that could have been used in my work. I will also include a section briefly touching on the 650 GHz capabilities of the Event Horizon Telescope.

On the Event Horizon Telescope collaboration website it is described that one of the

major concerns of performing 345 GHz observations is the atmospheric conditions, both in terms of water vapor which absorbs and re-emits radiation - adding noise in the form of sky brightness - but also in terms of troposphere fluctuations which result in phase corruption of the incoming signal. In my simulations, I have attempted to address both of these effects in a simplified sense: Atmospheric noise is incorporated into the site system-equivalent-flux-density using average atmospheric conditions and source elevations. Fluctuations are in reality eliminated by use of the two-stage ALMA approach, which I have replicated by pre-calibrating the signal in my simulations, before correlation. While these fixes should suffice for simulated 230 GHz observations, it is uncertain whether this is acceptable for simulated 345 GHz observations. It is stated on the EHT website, that "[...] most EHT sites have suitable weather for 345 GHz observing under normal winter conditions."[34], but ongoing measurements of atmospheric stability above the Thule site are still being carried out. Thus, the extent to which the Greenland Telescope is able to correlate the M87* flux, while located at Thule, is uncertain. The absence of Thule weather data is not only limited to troposphere stability (atmospheric coherence timescale measurements), but also opacity measurements in general. My estimated results for the 345 GHz opacity at Thule, that I have extrapolated based on 230 GHz estimates supplied by Matsushita et. al, argue that the current location of the Greenland Telescope is not limited by sky brightness to such a degree that it is unusable, but these are only estimates based on the simplified atmosphere transmission spectra generator ATRAN. Using a more deep atmosphere model such as *am*[35] would help validate these results, until more specific measurements are available.

The usage of several M87* models was another missed opportunity. As the model structure, on both small and large scales alike, play an important role in the recovered image, I would have liked to include more than one model. Ideally I would have liked to produce a variety of my own ring models, using radiative transfer software like RADMC-3D (2.0)[36], which is a free open-source software package used for radiative transfer calculations for objects such as protoplanetary disks, circumstellar envelopes and, most importantly, dusty tori around AGNs. As an example, varying source structure could help to reveal whether the drop in the ALMA-GLT baseline S/N gain rate, observed in my simulated 345 GHz observations, is an isolated case caused by the absence of small scale emission, and whether another source would change this fact. It would have been interesting as well, to further analyze the capabilities of EHT, when viewing other sources than M87*, such as the possibility of using the array for high resolution protoplanetary disk observations, although this is not likely, as the array is only sensitive to non-thermal radiation.

Aside from multiple models, I would have liked to make use of more than a singular imaging software, or algorithm. This approach was also used when imaging the M87* data

[34] `https://eventhorizontelescope.org/moving-towards-higher-observing-frequencies`
[35] https://lweb.cfa.harvard.edu/ spaine/am/index.html
[36] `https://www.ita.uni-heidelberg.de/~dullemond/software/radmc-3d/`

in 2017 (The EHT Collaboration et al. [2019c]). Initially, I was planning on using the regularized maximum likelihood (RML) imaging algorithm. This algorithm is also packaged with `eht-imaging`, but the inclusion would have been lackluster due to complexity and time-constraints. Aside from comparing my produced clean maps to my own blurred model images, comparisons between clean maps produced by different imaging software, such as the Python based SMILI[37] or software package AIPS[38] which both apply the CLEAN algorithm to sparse Fourier samples, would serve as extended image validation, should the results be similar. Unfortunately, these software require time to familiarize oneself with, which I was limited from doing due to time constraints. In the end I chose to focus on *one* imaging software package, namely DIFMAP, and how I could make it communicate with Python and `eht-imaging`.

Based on my examination of the background (off-source) standard deviation of my final clean maps, my DIFMAP cleaning script is not ideal. My final clean maps contain negative values that are in the same order-of-magnitude as the standard deviation, which will impact the recovered S/N ratio. Solutions to this, would be a cleaning script that does not allow for negative components in the residual map *or* a script which uses a decreased loop gain value. If these solutions were combined, the clean algorithm should subtract the dirty beam from the dirty map at more controlled levels, which could decrease minimum values to lower orders-of-magnitude, while keeping them above null, which would eliminate standard deviation increase due to negative values. Of course, implementations such as these come at the cost of increased run-time. I am unsure as to why the background standard deviation is increased in simulated observations following the GLT relocation; minimum image values, which do impact standard deviation, seem consistent within each observing frequency so this is not the likely explanation. It is most likely connected to the updated telescope position which is associated with slightly different visibility samples in the Fourier domain. Theoretical noise estimates predict that sensitivity is highest following relocation and the same conclusion is reached when using natural weighing of the visibility data.

650 GHz observations using the EHT array are most likely a ways off. Researching the capabilities of each telescope reveals that only very few sites are equipped with receivers that cover this frequency. These (and SEFD estimates[39]) include ALMA (1758 Jy), APEX (31860 Jy), SMA (39000 Jy), JCMT (15220 Jy) and the Greenland Telescope (73309 Jy) although the receiver is only proposed to work optimally at the Summit Site (see Table 6). Assuming these receivers can work in sub-mm VLBI observation configurations, I was *not* able to recover an acceptable image of M87* using the observation time frame used for my 230 GHz and 345 GHz simulations. To test the capability when observing at a frequency this high, I created a simple script that overwrote the M87* model image data with zero values

[37] `https://github.com/astrosmili/smili`

[38] `http://www.aips.nrao.edu/index.shtml`

[39] 650GHz sensitivities are estimated in the same manner as the 345GHz sensitivity.

before assigning values to two pixels, acting as points sources, at a user defined distance from the image center. The user also defines the total image flux, as well as the point source emission frequencies. In this way I could perform simple observations of separated point sources, while still maintaining the model header information about source position and observation date. For a double point source at the location of M87*, separated by 15 μas and a total source flux of 0.05 Jy for all observing frequencies, I simulated three observations utilizing same global parameters as for the M87* observations. For each observing frequency I include all available telescopes, with GLT located at the Summit Camp. The synthetic data was imaged using natural weighing of the visibility data for enhanced sensitivity, and clean models were finally restored with circular beams of sizes 20μas, 15μas and 10μas. Fig. 40 shows the recovered images.

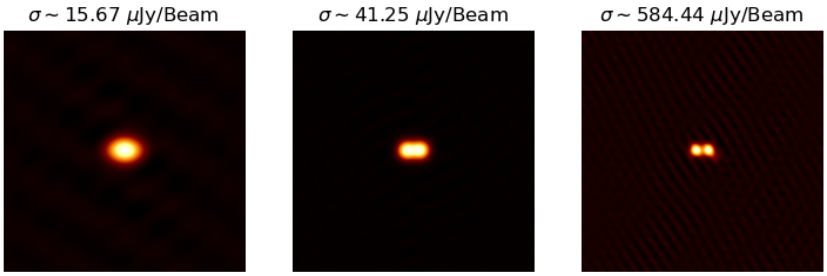

Figure 40: Simulated observations of a double point source, separated by 15μas. Total image flux is 0.05Jy. Observing frequency from left to right is 230GHz, 345GHz and 650GHz. Clean models are restored using circular gaussian beams of sizes (left to right) 20μas, 15μas and 10μas.

As expected the source is unresolved at 230 GHz and barely resolved at 345 GHz. The slight added details comes at the cost of an image noise increase of $\sim$ 163%, or about 2.5 times greater. At 650 GHz the image is resolved and each point source is seen as a separate entity. Noise is increased $\sim$ 3630% from 230 GHz and 1317% from 345 GHz (37 and 14 times greater respectively). This simple example shows the gain in observing at higher frequencies; improved resolution can potentially reveal structure that would otherwise be unresolved, but these simulations work under two major assumptions. Firstly, it is not plausible that the total flux of the image is unchanged over such a range of observed frequencies. Secondly, it is highly uncertain that integration times equal to those achievable during 230 GHz observations are possible during 650 GHz observations. This small example merely serves to illustrate the power of high frequency interferometric observations. The resolving power of the final image (650 GHz) would be equal to achieving a clear image of a single salt crystal in Copenhagen, if the photographer was setup in Skagen, as opposed to a muddy image of

two (345 GHz) or more ($\leq$ 230GHz).

7 Conclusion and outlook

Upon many months of building a deeper understanding, and appreciation, for radio interferometry and based on my work with atmospheric data and VLBI simulations I have reached the following conclusions:

The relocation of the Greenland Telescope will most assuredly improve year-round observing conditions for single dish observations, affecting all equipped receivers. Opacity estimates show that typical (75th percentile) Summer season conditions at the proposed new site, the Summit Camp, are marginally better than typical Winter season conditions at the current location. I estimate that the atmospheric transmission upgrades before *and* following the GLT relocation for Winter season are 81% $\implies$ 93% for the 230 GHz receiver, and 65% $\implies$ 76% for the 345GHz receiver. In terms of opacity these values are 0.210 $\implies$ 0.0801 (230 GHz) and 0.430 $\implies$ 0.272 (345 GHz). Typical Summer opacity values are decreased from 0.440 $\implies$ 0.159 (230 GHz) and 0.967 $\implies$ 0.565 (345 GHz). Furthermore, I estimate only a slight potential upgrade to the 230 GHz receiver SEFD following the relocation (12.5%), while the upgrade is more noticeable for the 345GHz receiver (42.8%). It is assumed that the 650 GHz and 850 GHz receiver on GLT are only operable at the proposed new site. These changes are in no doubt upgrades that allow for not only shorter integration times on both receivers and also allow for science observations for more parts of the year, but the numbers also indicate that the current position (Thule) is *not* limited by atmospheric opacity to such a degree that single dish 345 GHz observations are impossible, at least for parts of Winter (The 345 GHz receiver is greatly hindered during Summer at Thule). The question remains whether the atmosphere above the Thule site is stable to such a degree that 230 GHz (1.3 mm) and 345 GHz (870 μm) VLBI observations are possible. This issue is still being researched today and there is, as of yet, no data available to answer this question.

In my simulations, I have shown the importance of the GLT baselines in regard to additional uv-coverage. While it may be possible to recover okay images at 230 GHz without the inclusion of GLT, the additional baselines are crucial to recover images at 345 GHz. It is for this particular frequency (and upwards) that atmospheric stability becomes a significantly limiting factor. Assuming that future measurements deem the atmosphere above the Thule site stable enough for 230 GHz / 345 GHz VLBI observations, thermal noise of the receivers do not seem to be limiting factors for observing my used M87* model (given my observation parameters that mimic the 2017 observation of M87*). If the atmosphere proves too unstable for high frequency VLBI observations, I have shown that images recovered without the use of GLT baselines are not optimal, thus reaffirming the need for relocating GLT to

the proposed new site. I estimate only a very slight increase in EHT sensitivity following the relocation of GLT, but this was expected due to the small size of the telescope. My inspection of the individual GLT baselines revealed greater changes in sensitivity following the relocation, but only really significant for the 345GHz receivers. The upgraded GLT sensitivity will boost the S/N gain rate on all GLT baselines, allowing for faster signal build up, ensuring more detections. The uv-coverage remains largely unchanged following the relocation, due to the relative close distance between Thule and the Summit Camp on a Global scale. Utilizing my simple separated point sources example, I have shown the potential EHT capability to resolve scales down to $\sim 10\mu$as, but I was not able to recover any successful image of my M87* model. This is most likely due to poor uv-coverage, caused by the absence of several telescopes, as they are not equipped with 650 GHz receivers. The relocation of GLT is a necessity for the use of the 650 GHz (and 850 GHz) receivers.

The question of whether or not the relocation of the Greenland Telescope is *worth* it, is a difficult one to answer at present. The single dish telescope would surely see an important upgrade, but most of the potential functionality gained from the operation, still remains at the current site. Results from atmospheric measurements above the Thule site will help answer the question of how limited VLBI observations are, which will help to shape the answer. In the end I believe that the relocation is inevitable as GLT and EHT observations progress toward higher frequencies (> 345 GHz). Important considerations also include the cost and manpower required to operate GLT at such a remote location, not to mention the lack of convenient access if repairs are required; all logistical questions that would be interesting to research even further. Future Event Horizon Telescope observations at 345 GHz are not far off. The array will have the ability to resolve M87* at scales extremely close to the width of the BH event horizon. The Greenland Telescope should suffice as an important addition to the EHT network, either from Thule or the proposed new site, the Summit Camp. Observations such as these will supply astronomers with an image that should provide even greater insight into the formation of astrophysical jets as well as a clear image of one of the most massive and fantastical objects, known to man.

Acknowledgements

I would like to express my deepest appreciation to my advisor Jes K. Jørgensen, as well as my co-advisor Darach J. Watson, for the guidance, perspective and comments given throughout my work. I am also very grateful for the extensive help supplied by PhD. Sigurd Jensen in regard to technical help with software and the use of Linux based operating systems. I wish to thank Dr. Satoki Matsushita, who has kindly provided me with detailed information regarding the Greenland Telescope, needed to complete my work. Special thanks to astronomers around the world: Nimesh Patel, Micheal Bremer, Miguel Sanchez, Paul Ho, Giovanni Muscari and Ivan Marti-Vidal for taking the time to answer emails and for helping me find the information I sought.

References

R. D. Blandford and D. G. Payne. Hydromagnetic flows from accretion disks and the production of radio jets. , 199:883–903, June 1982. doi: 10.1093/mnras/199.4.883.

R. D. Blandford and R. L. Znajek. Electromagnetic extraction of energy from Kerr black holes. *Monthly Notices of the Royal Astronomical Society*, 179(3):433–456, 07 1977. ISSN 0035-8711. doi: 10.1093/mnras/179.3.433. URL https://doi.org/10.1093/mnras/179.3.433.

Avery E. Broderick and Abraham Loeb. IMAGING THE BLACK HOLE SILHOUETTE OF m87: IMPLICATIONS FOR JET FORMATION AND BLACK HOLE SPIN. *The Astrophysical Journal*, 697(2): 1164–1179, may 2009. doi: 10.1088/0004-637x/697/2/1164. URL https://doi.org/10.1088/0004-637x/697/2/1164.

C. L. Brogan, L. M. Pérez, T. R. Hunter, W. R. F. Dent, A. S. Hales, R. E. Hills, S. Corder, E. B. Fomalont, C. Vlahakis, and et al. The 2014 alma long baseline campaign: First results from high angular resolution observations toward the hl tau region. *The Astrophysical Journal*, 808(1):L3, Jul 2015. ISSN 2041-8213. doi: 10.1088/2041-8205/808/1/l3. URL http://dx.doi.org/10.1088/2041-8205/808/1/L3.

J. V. Buckle, R. E. Hills, H. Smith, W. R. F. Dent, G. Bell, E. I. Curtis, R. Dace, H. Gibson, S. F. Graves, J. Leech, and et al. Harp/acsis: a submillimetre spectral imaging system on the james clerk maxwell telescope. *Monthly Notices of the Royal Astronomical Society*, 399(2):1026–1043, Oct 2009. ISSN 1365-2966. doi: 10.1111/j.1365-2966.2009.15347.x. URL http://dx.doi.org/10.1111/j.1365-2966.2009.15347.x.

Andrew Chael, Ramesh Narayan, and Michael D Johnson. Two-temperature, Magnetically Arrested Disc simulations of the jet from the supermassive black hole in M87. *Monthly Notices of the Royal Astronomical Society*, 486(2):2873–2895, 04 2019. ISSN 0035-8711. doi: 10.1093/mnras/stz988. URL https://doi.org/10.1093/mnras/stz988.

Andrew A. Chael, Michael D. Johnson, Katherine L. Bouman, Lindy L. Blackburn, Kazunori Akiyama, and Ramesh Narayan. Interferometric imaging directly with closure phases and closure amplitudes. *The Astrophysical Journal*, 857(1):23, Apr 2018. ISSN 1538-4357. doi: 10.3847/1538-4357/aab6a8. URL http://dx.doi.org/10.3847/1538-4357/aab6a8.

James J. Condon and Scott M. Ransom. *Essential Radio Astronomy*. Princeton University Press, 2016.

H. D. Curtis. Descriptions of 762 Nebulae and Clusters Photographed with the Crossley Reflector. *Publications of Lick Observatory*, 13:9–42, January 1918.

Karl Gebhardt, Joshua Adams, Douglas Richstone, Tod R. Lauer, S. M. Faber, Kayhan Gültekin, Jeremy Murphy, and Scott Tremaine. The Black Hole Mass in M87 from Gemini/NIFS Adaptive Optics Observations. , 729(2):119, March 2011. doi: 10.1088/0004-637X/729/2/119.

Ciriaco Goddi, Ivan Marti-Vidal, Hugo Messias, Geoff Crew, Ruben Herrero-Illana, Violette Impellizzeri, Helge Rottmann, Jan Wagner, Ed Fomalont, Lynn D. Matthews, Dirk Petry, Neil Phillips, Remo Tilanus, Eric Villard, Lindy Blackburn, Michael Janßen, and Maciek Wielgus. Calibration of alma as a phased array: Alma observations during the 2017 vlbi campaign, 2019.

J.A. Högbom. Aperture synthesis with a non-regular distribution of interferometer baselines. 15, p. 417, June 1974.

Jes Kristian Jørgensen. Lecture 3: "telescopes, images and how to improve them", November 2019.

Satoki Matsushita, Keiichi Asada, Pierre L. Martin-Cocher, Ming-Tang Chen, Paul T. P. Ho, Makoto Inoue, Patrick M. Koch, Scott N. Paine, and David D. Turner. 3.5 year monitoring of 225 ghz opacity at the summit of greenland. *Publications of the Astronomical Society of the Pacific*, 129(972):025001, Dec 2016. ISSN 1538-3873. doi: 10.1088/1538-3873/129/972/025001. URL http://dx.doi.org/10.1088/1538-3873/129/972/025001.

Rendong Nan, Di Li, Chengjin Jin, Qiming Wang, Lichun Zhu, Wenbai Zhu, Haiyan Zhang, Youling Yue, and Lei Qian. The five-hundred-meter aperture spherical radio telescope (fast) project. *International Journal of Modern Physics D*, 20(06):989–1024, Jun 2011. ISSN 1793-6594. doi: 10.1142/s0218271811019335. URL http://dx.doi.org/10.1142/S0218271811019335.

J. Pety, J. Boissier, and E. Reynier. Noema time/sensitivity estimator, August 2015.

Melisa Prieto, Juan Fernández Ontiveros, S. Markoff, Daniel Espada, and O. Gonzalez-Martin. The central parsecs of m87: Jet emission and an elusive accretion disc. *Monthly Notices of the Royal Astronomical Society*, 457, 08 2015. doi: 10.1093/mnras/stw166.

A. Remijan, A. Biggs, P. Cortes, Dent A., B., J. Di Francesco, E. Fomalont, A. Hales, S. Kameno, B. Mason, N. Philips, K. Saini, F. Stoehr, B. Vila Vilaro, and E. Villard. Alma technical handbook, 2019.

The EHT Collaboration et al. First m87 event horizon telescope results. i. the shadow of the supermassive black hole. *ApJL*, 875:1, 2019a. URL https://iopscience.iop.org/article/10.3847/2041-8213/ab0ec7.

The EHT Collaboration et al. First m87 event horizon telescope results. ii. array and instrumentation. *ApJL*, 875:2, 2019b. URL https://iopscience.iop.org/article/10.3847/2041-8213/ab0c96.

The EHT Collaboration et al. First m87 event horizon telescope results. iv. imaging the central supermassive black hole. *ApJL*, 875:4, 2019c. URL https://iopscience.iop.org/article/10.3847/2041-8213/ab0e85.

A. Richard Thompson, James M. Moran, and George W. Swenson Jr. *Interferometry and Synthesis in Radio Astronomy*. Springer Open, 3 edition, 2017.

Feng Yuan and Ramesh Narayan. Hot accretion flows around black holes. *Annual Review of Astronomy and Astrophysics*, 52(1):529–588, Aug 2014. ISSN 1545-4282. doi: 10.1146/annurev-astro-082812-141003. URL http://dx.doi.org/10.1146/annurev-astro-082812-141003.

Appendix

Appendix A - Synthetic data generation script

```
### Simulate VLBI observation ###

# Import packages #
import os
import numpy as np
import ehtim as eh
from ehtim.calibrating import self_cal as sc
import matplotlib.pyplot as pl

# Clean last run
os.system('rm obs.uvp')
os.system('rm *.log*')
os.system('rm *.fits')
os.system('rm *.png')

print("### Setting up VLBI simulation using eht-image version:",eh.version,"###")

## Load model image and array config ##
im = eh.image.load_txt("./my_models/howes_m87_230GHz.txt") #230GHz
#im = eh.image.load_txt("./my_models/howes_m87_345GHz.txt") #345GHz
#im = eh.image.load_fits("./my_models/650GHz.fits") #650GHz

#im = eh.image.load_fits("./seperated_point/sep_points.fits") #FOR POINT SOURCE VERSION

array = eh.array.load_txt("./my_arrays/230GHz/WGS84_eht_thule.txt") #My 2020 CONFIG
#array = eh.array.load_txt("./From Software/arrays/EHT2017.txt") #2017 M87 Config

#im.display()
im.save_fits('model_image.fits')

## Observation parameters ##
tint_sec = 30*10
tadv_sec = 1200
tstart_hr = 1
tstop_hr = 9
bw_hz = 4e9

snr_cut = 3

obs = im.observe(array, tint_sec, tadv_sec, tstart_hr, tstop_hr, bw_hz,
                 ampcal=True, phasecal=True,add_th_noise=True).flag_low_snr(snr_cut)
beam_params = obs.fit_beam()
avg_width = (2*beam_params[0]+beam_params[1])/3
```

```
print("\nAverage Beam Radius: %.2f micro arc sec!" %(avg_width*206264806719))

im.blur_circ(avg_width).save_fits("blurred_model.fits") #Create blurred Model Image for reference


corr_t = (tstop_hr - tstart_hr)*3600/tadv_sec * tint_sec
print('\n## OBS PARAMS ##')
print('Estimated total correlation time is %.2f seconds, or %.2f minutes' %(corr_t,corr_t/60))

## Print observation parameters ##
print("Integration time is",tint_sec,"second(s)")
print("Time between scans is",tadv_sec,"second(s)")
print("Campaign starts at",tstart_hr,"and ends at",tstop_hr,"hours")
print("bandwidth is %.2f GHz" %(bw_hz*1e-9))
print('###\n')

#input("Run simulation? Else Ctrl-Z\n")

obs.plotall("u","v",conj=True,export_pdf="uvcov.png",show=False,grid=False,
        rangex=False,rangey=False, markersize=6,tag_bl=False,legend=False,color="red") #UVcov
obs.plotall("uvdist","amp",marker='k.',export_pdf="vis.png",show=False) #Visibility
obs.save_uvfits('obs.uvp') #Generate observation file for Difmap CLEAN use
print("### Done! ###")
```

Appendix B - DIFMAP cleaning script

```
obs obs.uvp
select

! Set Expected flux of source
uvzero 1,10

! Set Uniform Weighing of data
uvw 2,-1

! Set Natural Weighing of data
!uvw 0,-2

! Set Mapsize
mapsize 1024, 0.0005


!Export Dirty Map and Beam
wbeam dirty_beam.fits
wdmap dirty_map.fits

clean -1000
selfcal
clean -5000
```

```
selfcal
clean −15000
selfcal true, true, 900


!radpl
restore %1
wdmap residual_map.fits
wmap clean_map.fits

exit
```

Appendix C - Python plotting script

```
## Script for displaying simulation results
## Requires .fits files from DIFMAP imaging (@simple_clean.txt)

## Import packages
import matplotlib.pyplot as pl
import matplotlib.patches as patches
import numpy as np
from astropy.utils.data import get_pkg_data_filename
from matplotlib.patches import Ellipse
from mpl_toolkits.axes_grid1.anchored_artists import AnchoredSizeBar
from astropy.io import fits
from astropy import stats
import matplotlib.font_manager as fm
fontprops = fm.FontProperties(size=15)

#Model
mod = fits.open(get_pkg_data_filename("model_image.fits"))[0]
mod_data = mod.data
mod_hdr = mod.header

mfreq = mod_hdr["FREQ"] #Hz
c = 2.99e+8 #m/s
mwave_cm = (c / mfreq) * 100 #cm

print("Measuring %.2f mm emission" %(mwave_cm * 10))

#Help Functions
def rms(x): return np.sqrt(np.mean(x**2)) #Root−mean−square calculation

def deg2as(x):
        return (x*3600) #Convert deg to arcsec

def my_fits_import(filename): #Function for easy .fits import
        x = fits.open(get_pkg_data_filename(filename))[0]
        data = x.data[0,0,:,:]
```

```
    hdr = x.header
    return data,hdr

def I2T(I_mJy,bmin_as,bmaj_as,w_cm=mwave_cm): #Convert to Brightness Temp.
    #UNIT SPECIFIC FORMULA!
    # I [mJy/Beam]
    # bmin ["]
    # bmax ["]
    T_b = 1.36 * (w_cm**2/(bmaj_as*bmin_as)) * I_mJy
    return T_b

## Data Import ##
cln_data, cln_hdr = my_fits_import("clean_map.fits") #Import CLEAN map
dmap_data, dmap_hdr = my_fits_import("dirty_map.fits") #Import Dirty map
res_data, res_hdr = my_fits_import("residual_map.fits") #Import Residual map
dbeam_data, dbeam_hdr = my_fits_import("dirty_beam.fits") #Import Dirty Beam
bmod_data = fits.open(get_pkg_data_filename("blurred_model.fits"))[0]

## Beam Params ##
bmaj = deg2as(cln_hdr["BMAJ"]) #Clean beam major axis [as]
bmin = deg2as(cln_hdr["BMIN"]) #Clean beam minor axis [as]
bpa = cln_hdr["BPA"] #Clean beam position [deg]

pixsize = cln_hdr["CDELT2"] #Pixelsize [deg/pix]

bmaj_pix = cln_hdr["BMAJ"]/-pixsize #[Pix]
bmin_pix = cln_hdr["BMIN"]/pixsize #[Pix]

## PLOTS ##
pl.figure(figsize=(12,12))

pl.subplot(221) #DIRTY MAP
pl.title(r'DM) rms: %.2e K' %I2T(rms(dmap_data)*1e+3,bmin,bmaj))
pl.imshow(I2T(dmap_data*1e+3,bmin,bmaj),cmap="afmhot",origin="lower")
pl.axis("off")
pl.colorbar(label="Brightness Temperature [K]")

pl.subplot(222) #DIRTY BEAM
pl.title(r'DB) $\sigma_{rms}$ = %.2e K' %(I2T(dbeam_hdr["NOISE"]*1e+3,bmaj,bmin)))
pl.imshow(dbeam_data,cmap="afmhot",origin="lower")
pl.axis("off")
pl.colorbar(label="PSF Response")
pl.xlim(512-256,512+256)
pl.ylim(512-256,512+256)

pl.subplot(223) #RESIDUAL MAP
pl.title('RM) rms: %.2e K' %(I2T(rms(res_data)*1e+3,bmin,bmaj)))
pl.imshow(I2T(res_data*1e+3,bmin,bmaj),cmap="afmhot",origin="lower")
```

```
pl.axis("off")
pl.colorbar(label="Brightness Temperature [K]")

pl.subplot(224) #CLEAN MAP
pl.title(r'CM) S/N $\sim %i$, rms: %.2e K' %(cln_hdr["DATAMAX"]/np.std(cln_data[400:480,50:130]),
    ↪ I2T(rms(cln_data)*1e+3,bmin,bmaj))) #Max Signal
ax = pl.gca()
pl.imshow(I2T(cln_data*1e+3,bmin,bmaj),cmap="afmhot",origin="lower")
pl.axis('off')
pl.colorbar(label='Brightness Temperature [K]')

cbm = Ellipse(xy=(50,50),width=bmin_pix,height=bmaj_pix,angle=bpa,color='w',fc='gray')
ax.add_patch(cbm)

rect = patches.Rectangle((50, 400), 80, 80, linewidth=1, edgecolor='r', facecolor='none')
ax.add_patch(rect)

reg = cln_data[400:480,50:130] #Off-source region
reg_rms = np.sqrt(np.mean(reg**2))

barlength = 70

scalebar = AnchoredSizeBar(ax.transData,
                           barlength, r'%i $\mu$as' %(barlength*deg2as(pixsize)*1e+6), 'lower_right',
                           pad=0.1,
                           color='white',
                           frameon=False,
                           size_vertical=2,
                           fontproperties=fontprops)

ax.add_artist(scalebar)
pl.savefig('results.png')

print("\n### S/N ###")
print("Max image value is %.3f Jy/Beam" %(cln_hdr["DATAMAX"]))
print("Min image values is %.2E Jy/Beam" %(cln_hdr["DATAMIN"]))
print("Std of bagground region is %.2E Jy/Beam" %(np.std(reg)))
print("[ABS. Std of bagground region is %.2E Jy/Beam]" %(np.std(np.abs(reg))))
print("(Estimated rms noise is %.2E)" %(cln_hdr["NOISE"]))
print("{Calculated region rms is %.2E}" %reg_rms)

print("\nS/N using std is %.2f (Theoretical: %.2f)" %(cln_hdr["DATAMAX"]/np.std(reg),cln_hdr["
    ↪ DATAMAX"]/cln_hdr["NOISE"]))
print("[S/N using ABS. std is %.2f]" %(cln_hdr["DATAMAX"]/np.std(np.abs(reg))))
print("{S/N using rms of region is %.2f}" %(cln_hdr["DATAMAX"]/reg_rms))
print("####\n")

#pl.show()
```